Hadronization at 12 GeV

Master's thesis
Paul van der Nat

July 2002

vrije Universiteit amsterdam

Contents

The price of asymptotic freedom is infrared slavery!

Chapter 1

Introduction

In deep inelastic scattering (DIS) a lepton, e.g. a positron, interacts through the exchange of a virtual photon with a quark (antiquark) inside a nucleon. The struck quark is knocked out of the nucleon and will form a hadron within a very short time period because of color confinement. This process of hadron formation is up to this moment not very well understood. It is not possible to calculate it in perturbative Quantum ChromoDynamics (pQCD), since it takes place at kinematics where pQCD is not applicable (see appendix A). Therefore, it is necessary for theorists to rely on phenomenological models. Experimentally, hadronization cannot be studied directly. Only the resulting (colorless) hadrons can be measured. Embedding the hadron formation process inside a nuclear environment offers a way to investigate this process. It is observed that the number of hadrons measured per DIS event is smaller for scattering on a large nucleus as compared to a small nucleus like the deuteron. A possible explanation is that the struck quark and the formed hadron reinteract with nucleons inside the nucleus.

The attenuation of the number of hadrons depends on the distance the quark traveled through the nucleus before it formed a hadron. Therefore, measuring this attenuation can give insight on the formation time of the hadron. The formation time is an important physical property characterizing a specific hadron type (for example a pion or a proton).

In this master's thesis the hadron attenuation is investigated. It is studied for a nitrogen target as well as for a krypton target in order to obtain the A dependence of the formation time of hadrons. The experiment was done using a 12 GeV positron beam energy and a fixed gas target. The result is compared to theoretical models and to a similar analysis, where a 27.5 GeV positron beam was used in the experiment.

This report is organized in the following way:

In chapter 2, first the DIS formalism is introduced, after which several aspects of hadronization are discussed. The chapter ends with a description of some phenomenological models. The subject of chapter 3 is the experimental setup. In the first part of chapter 4 the analysis is discussed and in the second part the obtained results are presented. Conclusions are drawn in chapter 5.

Chapter 2

Hadron formation

Introduction

In lepton-nucleon scattering a lepton interacts with a nucleon through the exchange of a virtual photon. A virtual photon is a photon with a non-zero mass, i.e. it does not obey the relation $E = pc$, in contrast with normal light. This virtual photon can only exist for a very short time period according to Heisenberg's uncertainty relation $\Delta t = \hbar/\Delta E$. If the incoming lepton looses a very large amount of energy in the scattering process, it can interact with individual quarks inside the nucleon. The quarks can then be knocked out of the nucleon. This is called deep inelastic scattering. The quark that is knocked out of the nucleon will combine with other quarks into a hadron. Hadron formation (or fragmentation) is the process during which the hadron is formed, from the moment the struck quark is knocked out of the nucleon till the moment that the hadron is formed.

Within this chapter various aspects of hadron formation and in particular hadron formation inside a nuclear environment are addressed. First, in section 2.1 the concept of inclusive and semi-inclusive scattering will be introduced, as well as the kinematic variables involved.

2.1 Kinematics

2.1.1 Inclusive scattering

A lepton scattering process is called inclusive if only the outgoing lepton is detected. Other particles produced in the scattering process are not considered.

The kinematics of the inclusive scattering process can be described by three independent four-vectors. For example, the vectors k, p and q can be chosen as shown in the Feynman diagram in Fig. 2.1.

Six independent Lorentz invariant quantities can be constructed from these three four-vectors: k^2, p^2, q^2, $k \cdot p$, $k \cdot q$ and $p \cdot q$. Two of them are just the masses of the particles involved ($k^2 = m_e^2$ and $p^2 = M^2$, respectively the mass of the lepton and the mass of the nucleon), two others depend on the energy of

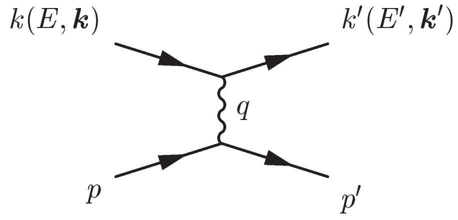

Figure 2.1: Feynman diagram describing inclusive scattering of a lepton off a nucleon.

the lepton-nucleon system and the scattering angle ($k \cdot p$ and $k \cdot q$). Therefore, two invariants are left to describe the interaction of the virtual photon with the target:

$$q^2 \overset{\text{LAB}}{=} -4EE' sin^2(\theta/2) \tag{2.1}$$

$$\frac{p \cdot q}{M} \equiv \nu \overset{\text{LAB}}{=} E - E', \tag{2.2}$$

with θ being the scattering angle and q^2 the invariant mass squared of the virtual photon (usually $Q^2 \equiv -q^2$ is used, which is always positive). The equations are valid within the laboratory (LAB) frame.

Alternatively, the two dimensionless variables x and y can be used:

$$x \equiv \frac{q^2}{2p \cdot q} = Q^2/2M\nu \tag{2.3}$$

$$y = \frac{p \cdot q}{p \cdot k} \overset{\text{LAB}}{=} \frac{E - E'}{E} \tag{2.4}$$

The *Bjorken* variable x can be interpreted as the momentum fraction of the nucleon carried by the struck quark, while y represents the energy fraction of the virtual photon.

The invariant mass squared of the final hadronic state is given by:

$$W^2 \equiv (p + q)^2 = (p')^2 = M^2 + 2M\nu - Q^2 \tag{2.5}$$

2.1.2 Semi-inclusive DIS

A deep inelastic scattering process is called semi-inclusive if besides the scattered lepton, at least one final hadron is also detected.

A dimensionless kinematic variable is introduced to describe the final hadron:

$$z = \frac{p \cdot p^h}{p \cdot q} \overset{\text{LAB}}{=} \frac{E^h}{E - E'}, \tag{2.6}$$

with p^h and E^h respectively the four-vector and the energy of the hadron. The variable z represents the fraction of the virtual photon energy transfered to this hadron.

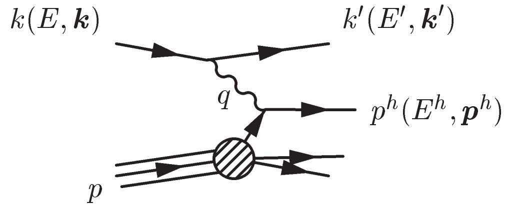

Figure 2.2: Schematic diagram describing **semi-inclusive** deep-inelastic scattering of a lepton off a nucleon.

2.2 Hadronization

When the struck quark leaves the nucleon, the color lines of force are stretched between this quark and the part of the nucleon that is left behind (called the nuclear *remnant*). This will increase the attraction trying to pull the quark back in the hadron. However, the result is not that the struck quark recombines into the original nucleon. The struck quark decelerates by the strong force trying to pull it back. Because of this deceleration the quark radiates gluons, just like decelerating/accelerating electrons radiate photons (Bremsstrahlung) [13]. The radiated gluons will then form a jet of hadrons, consisting mostly of pions. It is most likely that pions are radiated, because pions are light mesons held together by rather short force lines (≈ 1 fm)[1]. The struck quark will also form a hadron in combination with one or two quarks originating from the color field. The hadron that contains the struck quark is called the leading hadron.

The final stable hadrons can be divided in three groups according to the type of process they originate from: hadrons from current fragmentation, from target fragmentation or from central fragmentation. Current fragmentation means the fragmentation of the struck quark (containing the leading hadron), target fragmentation is the fragmentation of the nuclear remnant and central fragmentation stems from fragmentation of the high density color field between the nuclear remnant and the struck quark. Leading hadrons have on average higher values of z than the hadrons resulting from current and target fragmentation. The objective of this analysis is to obtain the formation time of the *leading* hadrons.

2.3 Hadron attenuation

When the process of hadronization, as discussed in the previous section, is embedded in a nuclear environment, it is influenced by quark energy loss through multiple scattering and gluon radiation as the struck quark propagates through the medium. The number of hadrons per DIS event, the hadron multiplicity, is smaller for scattering from a large nucleus compared to scattering from a smaller nucleus like the deuteron. The effect of hadron attenuation is studied

[1] Pions are the lightest hadrons and therefore easily formed. Up to about 1972 pions were even thought to be the mediators of the strong force.

through the attenuation ratio, which is defined as a function of ν and z as:

$$R_{att}(z,\nu) = \frac{\left(\frac{1}{d\sigma(e,e')/d\nu} \frac{d\sigma(e,e'h)}{dzd\nu}\right)_A}{\left(\frac{1}{d\sigma(e,e')/d\nu} \frac{d\sigma(e,e'h)}{dzd\nu}\right)_D} = \frac{N_h^A(z,\nu)\ /\ N_e^A(\nu)}{N_h^D(z,\nu)\ /\ N_e^D(\nu)}, \tag{2.7}$$

with $\sigma(e,e')$ and $\sigma(e,e'h)$ respectively the inclusive cross section and the semi-inclusive cross section. In this equation A refers to the nuclear target under investigation (krypton or nitrogen in this analysis) and D refers to deuterium. The ratio of multiplicities expresses the relative effect of hadron attenuation on nucleus A with respect to the deuteron. The semi-inclusive cross sections are divided by the inclusive cross sections to separate the A-dependence of the semi-inclusive process from the A-dependence of the inclusive process. The right hand side of Eq. (2.7) shows that the attenuation ratio can be expressed in terms of measured yields. Here, $N_h(z,\nu)$ is the number of hadrons for a certain (ν,z)-interval and $N_e(\nu)$ the number of DIS events for the same ν-interval.

If the final hadron is formed within the ^{84}Kr or ^{14}N nucleus, also hadron-nucleon scattering inside the nucleus has to be taken into account. This leads to a larger hadron attenuation. The size of the attenuation depends on the distance the hadron moves through the nucleus, which is related to the formation time of the hadron. Fig. 2.3 shows a schematic representation of the process of hadron formation.

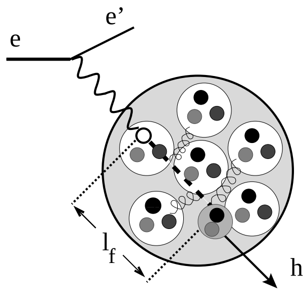

Figure 2.3: Schematic representation of hadronization in a nuclear medium.

2.4 Cross sections

In this section expressions for the inclusive and semi-inclusive cross sections are given. These expressions are used in section 2.5 to define the attenuation ratio in terms of fundamental properties of the quarks.

2.4.1 Inclusive cross section

The inclusive cross section is given by:

$$\frac{d\sigma(e,e')}{dE'd\Omega} = \frac{\alpha^2}{q^4}\frac{E'}{E}L_{\mu\nu}W^{\mu\nu}, \tag{2.8}$$

where $\alpha = e^2/4\pi\hbar c$. The tensor $L_{\mu\nu}$ describes the lepton vertex, while $W^{\mu\nu}$ describes the hadron vertex. The lepton tensor can be exactly calculated in QED. The hadron tensor cannot be calculated in pQCD, since the hadron formation takes place at too low values of Q^2 for pQCD to be applicable. However, the tensor $W^{\mu\nu}$ can be parameterized in terms of the structure functions of the nucleon ($F_1(\nu, Q^2)$ and $F_2(\nu, Q^2)$) by requiring parity conservation and time reversal invariance of the strong interaction as well as current conservation at the hadron vertex. (See for instance [7] or [13].) These structure functions describe the electromagnetic structure of the nucleon. Since the virtual photon only couples to particles that carry electric charge, the structure functions describe the structure of the nucleon with respect to the charged particles inside. The difference between F_1 and F_2 originates from the two possible polarization states of the mediating photon, respectively transverse and longitudinal. "The structure functions parameterize our total ignorance of the hadronic current." [13] They are obtained experimentally.

Contraction of the two tensors $L_{\mu\nu}$ and $W^{\mu\nu}$ gives for the unpolarized inclusive cross section:

$$\left.\frac{d\sigma}{dE' d\Omega}\right|_{\mathrm{LAB}} = \frac{\alpha^2}{4E^2 \sin^4 \frac{\theta}{2}} \left\{ F_2(\nu, Q^2) \cos^2 \frac{\theta}{2} + 2F_1(\nu, Q^2) \sin^2 \frac{\theta}{2} \right\}. \qquad (2.9)$$

Rewritten as a function of the dimensionless variables x-Bjorken and y this gives:

$$\left.\frac{d\sigma}{dx dy}\right|_{\mathrm{LAB}} = \frac{2\pi\alpha^2}{x^2 y^2 M E} \left\{ x y^2 F_1(x, Q^2) + \left[(1-y) - \frac{Mxy}{2E} \right] F_2(x, Q^2) \right\}. \quad (2.10)$$

2.4.2 Semi-inclusive cross section

The semi-inclusive DIS cross section can be written as

$$\frac{d\sigma(e, e'h)}{dz} = \sum_i \sigma(e, e'q_i) D_i^h(z), \qquad (2.11)$$

where the quark fragmentation function $D_i^h(z)$ gives the probability for a quark of type i to form a hadron h carrying a fraction z of the quark's energy. The variable $\sigma(e, e'q_i)$ represents the cross section for scattering off a certain quark type i.

In Eq. (2.11) it is assumed that the probability for the struck quark to form a certain hadron is independent of the way the quark was produced. This is an approximation called *factorization*.

2.5 The quark parton model

In the naive quark parton model it is assumed that the constituents of the nucleon (partons) are *non-interacting* point-like spin-1/2 particles, i.e. non-interacting quarks (antiquarks). Deep-inelastic scattering is seen as elastic scattering off the partons. The structure functions of the nucleon can then be written as the sum over the structure functions of its constituents. As a consequence, the structure functions F_1 and F_2 are closely related. They are given by the Callen-Gross relation as:

$$2xF_1(x) = F_2(x) = x \sum_i e_i^2 q_i(x) \tag{2.12}$$

where the sum is over all charged partons (quarks and antiquarks, $i = u$, d, s, $\bar{u}$, $\bar{d}$, $\bar{s}$ etc.), e_i is the quark (antiquark) charge. The variable $q_i(x)$ is the quark distribution function, which represents the probability that a quark (antiquark) of type i carries a fraction x of the nucleon's momentum. Note that the structure functions only depend on x and not on Q^2 and ν separately anymore. This is called *Bjorken scaling*, which reflects the fact that the partons are effectively seen as point-like particles.

Within the quark parton model Eq. (2.10) for the inclusive cross section can be written as:

$$\frac{d\sigma}{dxdy} = \frac{2\pi\alpha^2}{xy^2ME}\left\{\frac{y^2}{2} + \left[(1-y) - \frac{Mxy}{2E}\right]\right\}\sum_i e_i^2 q_i(x). \tag{2.13}$$

In order to obtain an expression for the hadron multiplicity the semi-inclusive cross section (Eq. (2.11)) is divided by the inclusive cross section, giving:

$$\frac{1}{\sigma(e,e')}\frac{d\sigma(e,e'h)}{dz} = \frac{\sum_i \sigma(e,e'q_i)D_i^h(z)}{\sum_i \sigma(e,e'q_i)}. \tag{2.14}$$

In the quark parton model this can be rewritten using Eq. (2.13) as:

$$\frac{1}{\sigma(e,e')}\frac{d\sigma(e,e'h)}{dz} = \frac{\int dx \sum_i e_i^2 q_i(x) D_i^h(z)}{\int dx \sum_i e_i^2 q_i(x)} \tag{2.15}$$

Eq. (2.15) can be used to write the attenuation ratio as a function of the energy fraction of the hadron z:

$$R_{att}(z) = \left[\frac{1}{\sigma(e,e')}\frac{d\sigma(e,e'h)}{dz}\right]_A \Bigg/ \left[\frac{1}{\sigma(e,e')}\frac{d\sigma(e,e'h)}{dz}\right]_D \tag{2.16}$$

$$= \left[\frac{\int dx \sum_i e_i^2 q_i(x) D_i^h(z)}{\int dx \sum_i e_i^2 q_i(x)}\right]_A \Bigg/ \left[\frac{\int dx \sum_i e_i^2 q_i(x) D_i^h(z)}{\int dx \sum_i e_i^2 q_i(x)}\right]_D \tag{2.17}$$

This equation relates the attenuation ratio to quark fragmentation functions within the quark parton model and with the assumption of factorization. Within the quark parton model the attenuation ratio will be equal to one. If the hadronization process is influenced by the nuclear medium, the variables $D_i^h(z)$ and $q_i(x)$ will be dependent on the atomic number A.

Note that this expression does not include a contribution from nuclear absorption (hadron-nucleon scattering inside the nucleus). This would require an additional A-dependent term. Therefore, this expression (Eq. (2.17)) is valid only if the final hadron is formed outside of the nucleus.

Scaling violations The quark parton model is an approximation. The partons must be *interacting* particles, otherwise they would not be confined inside a nucleon. A more precise picture is given in QCD. The nucleon contains three *valence* quarks, bound together by the exchange of gluons. These gluons can fluctuate into quark-antiquark pairs. Besides these quarks and gluons arising from the interaction between the valence quarks, all three quarks are surrounded by quarks, antiquarks and gluons from vacuum polarization (see appendix A).

Gluon radiation involved in vacuum polarization cause Bjorken scaling to be violated. It has indeed been measured in experiments that F_2 depends on x and Q^2 separately. With increasing Q^2, F_2 increases at small x and decreases at large x. This Q^2 dependence of F_2 can be calculated by the Altarelli-Parisi evolution equation [13].

2.6 Theoretical models

In this section some phenomenological models describing hadronization in a nuclear environment are discussed. Calculations of the attenuation ratio are available for the kinematics of the HERMES experiment from three of these models: the flavor dependent model [4], the rescaling model [1] and the gluon-bremsstrahlung model [16]. For this last model, calculations are only available for the 27 GeV data, not for the 12 GeV data. As an introduction, first some basic properties of the Lund string model [20] and the two-time scale model [32] are explained, because the flavor dependent model and the rescaling model are closely related to these models.

Lund string model The Lund string model [20] is one of the first models to describe hadronization. It describes the stretching of the color field between the struck quark and the nuclear remnant by a one-dimensional classical object, a string. The energy stored in the string is proportional to the length, given by the string tension $\kappa \approx 1$ GeV/fm. The gluon-radiation is pictured as a breaking of the string into smaller strings, corresponding to $q\bar{q}$-pairs. This breaking of strings continues untill an additional $q\bar{q}$-pair would not have enough energy left to form a meson. This process is schematically shown in Fig. 2.4. Baryon formation can also be described with this model, which involves the breaking of the string into diquark-antidiquark pairs.

Two-time scale model In this extension to the Lund string model [32] it is recognized that the constituents of a hadron are not formed at the same time, but are created during the hadronization process. Therefore, the process is divided into two time scales. This is shown schematically in Fig. 2.5. The time period τ_c is the time between the virtual photon exchange and the moment the first constituent of the hadron is created. The time period τ_h is the time it takes to form the final hadron. These time periods are related to two different cross sections, σ^* and σ_c. The cross section σ^* is related to the interaction of the initial color string with the nuclear environment. The cross section σ_c corresponds to the interaction of a pre-hadronic state with the nuclear medium.

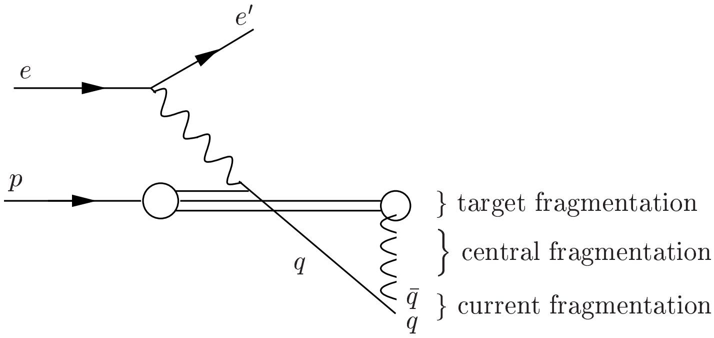

Figure 2.4: The formation of $q\bar{q}$ pairs through string breaking. The different fragmention regions are also indicated.

Once the hadron is formed it will interact with the medium with a cross-section σ_h.

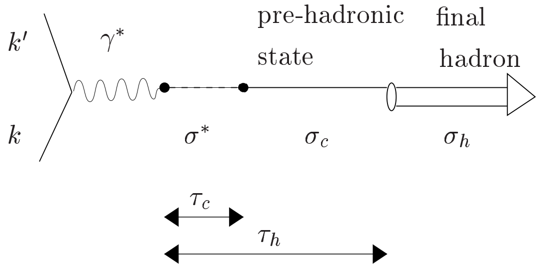

Figure 2.5: Schematic representation of the two-time scale model

The model predicts a dependence of the formation time on the hadron energy according to:

$$\tau_h - \tau_c = \frac{E_h}{\kappa c} = \frac{z\nu}{\kappa c}, \tag{2.18}$$

where $= \nu/\kappa$ is equal to the total length of the Lund string, $L = \nu/\kappa$. The formation times are given in the target rest frame. Using that $0 \leqslant z \leqslant 1$ it is predicted that:

$$0 \leqslant \tau_c \leqslant \frac{(1-z)}{c}\frac{\nu}{\kappa} \tag{2.19}$$

$$\frac{z\nu}{c\kappa} \leqslant \tau_h \leqslant \frac{1}{c}\frac{\nu}{\kappa}. \tag{2.20}$$

Therefore, the model predicts the maximum formation time (of the final hadron) to be:

$$\tau_h^{\max} = \frac{\nu}{\kappa c}, \tag{2.21}$$

which corresponds to the formation time τ_h in the limit $z \to 1$. An important prediction from this model is that if the pre-hadronic state between τ_c and τ_h

already interacts with a significant cross section σ_c with the nuclear environment, that the attenuation will increase with increasing z. (With increasing z, τ_c decreases resulting in a longer time for the pre-hadronic state and the final hadron to interact within the nucleus.)

Flavor dependent model This model [4] is based on the Lund string model and the two-time scale model. The model only describes mesons, baryons are not included. Also in this model the string tension is chosen to be $\kappa \approx 1$ GeV/fm. An important difference with other models is that it explicitly takes into account the flavor content and charge of the hadrons produced in the fragmentation process. The model describes the fragmentation of the three fastest hadrons on the string and therefore the model is applicable within a wide range of z, i.e. $z > 0.1 - 0.2$.

In the string model it is assumed that the fast end of the string always contains a quark, not an antiquark, which is only true in the valence range $x_{bj} > 0.2$. However in the flavor dependent model, also the possibility that the fast end of the string contains an antiquark is taken into account.

For the nuclear absorption *total* cross sections are used, meaning that the cross section includes inelastic as well as elastic scattering. In particular, for pions $\sigma_{\pi^+} = \sigma_{\pi^-} = 25$ mb is used and for kaons $\sigma_{k^+} = 17$ mb and $\sigma_{k^-} = 23$ mb.

The model uses the following average formation time for the leading hadron:

$$\tau_h = (1 - z)\frac{\nu}{\kappa c} \ , \tag{2.22}$$

which corresponds to the maximum constituent formation time of the two-time scale model, see Eq. (2.19).

Rescaling model This model [1] is also based on the Lund string model and the two-time scale model and it also describes only the attenuation of mesons. The most important characteristic of this model is the assumption of a change in the confinement scale of the nucleons inside a nucleus. The explanation for this behavior is that the nucleons inside a nucleus overlap, allowing quarks and gluons to propagate over longer distances than in an isolated nucleon. This affects both the quark distribution functions $q_i(x)$ and the quark fragmentation functions $D_i^h(z)$, introduced in section 2.5 and section 2.4.2 respectively.

The model uses a rather small string constant compared to other models $\kappa = 0.25 - 0.4$ GeV/fm. It is assumed that the cross section of the initial color string $\sigma^* = 0$ mb. For the cross section of the final hadron this model uses the *inelastic* hadron-nucleon cross sections. For pions $\sigma_{\pi^+} = 20$ mb and $\sigma_{\pi^-} = 22$ mb is used and for kaons $\sigma_{k^+} = 14$ mb and $\sigma_{k^-} = 20$ mb. The cross section of the pre-hadronic state is assumed to be equal to the cross section of the final hadron, i.e. $\sigma_c = \sigma_h$. With this assumption the model only needs to consider the formation time τ_c of the pre-hadronic state. It is given by:

$$\tau_c = \left[\frac{-\ln(z^2) - 1 + z^2}{1 - z^2}\right]\frac{z\nu}{\kappa}. \tag{2.23}$$

In the limit $z \to 1$, this gives the same dependence on the kinematic variables ν and z as the flavor dependent model $\tau_c \to (1-z)\frac{\nu}{\kappa c}$. In this limit, the only difference comes from the string constant κ.

Gluon-Bremsstrahlung model In this model [16, 17] only the attenuation of fast forward mesons (containing the struck quark) is described, $z > 0.5$. The model calculates the energy that the virtual quark looses through gluon radiation untill the final meson is formed. It is assumed that the leading meson originates from a $q\bar{q}$ dipole, where the antiquark comes from the last emitted gluon. The model also takes into account color transparency [5], causing a reduced interaction probability of the initial $q\bar{q}$ pair . According to the model the gluon radiation can only explain a very small part of the total attenuation. The largest contribution comes from hadron-nucleon scattering inside the nucleus. Calculations were done for a 27 GeV beam energy and for those kinematics it was concluded that the combined contributions of gluon radiation and color transparency can explain only $2-3\%$ of the total attenuation [29]. Therefore, according to this model the hadron is formed within the nucleus and most of the attenuation is coming from nuclear absorption.

The model predicts the following expression for the energy loss of the quark through gluon radiation:

$$\frac{dE}{dt} = \frac{-\epsilon\nu(1-z)}{t}, \tag{2.24}$$

where $\epsilon = 4\alpha_s(k_T^2)/3\pi$ with α_s the running coupling constant (see appendix A) and k_T the transverse momentum of the emitted gluons. This energy loss is fixed to be equal to the string tension[2] $dE/dt \approx 1$ GeV/fm. From equation 2.6 the following expression for the formation time is derived [16, 17]:

$$\tau_h = c_h\nu(1-z), \tag{2.25}$$

where c_h is a constant, which is characteristic for the type of formed hadron ($c_h = 1.35$ fm/GeV$\cdot c$ for pions).

The $(1-z)$-dependence is motivated by the following reasoning. If a meson has a large value of z, this indicates that the struck quark did not emit many gluons. In the model, the quark radiates gluons untill the final meson is formed and therefore a high z meson will correspond to a short formation time. This meson will then have a longer time to interact with the nucleus' constituents, giving rise to a larger attenuation. For the cross section, related to the nuclear absorption, the model uses the weighted sum of the individual total meson cross sections, $\sigma_h \approx 25$ mb [12].

Predictions from the rescaling model, the flavor dependent model and the gluon-bremsstrahlung model for the attenuation ratio versus ν and z are presented in sec. 4.5 where they are compared with the results of this analysis.

[2]Therefore, this model is also indirectly related to the string model.

Chapter 3

The HERMES experiment

The main goal of the HERMES experiment (HERA MEasurement of Spin) is to study the spin structure of the nucleon. The HERMES experiment is a deep-inelastic scattering experiment, for scattering of (longitudinally) *polarized* electrons or positrons off a *polarized* gas target. However, for the analysis presented in this master's thesis unpolarized targets were used. For that reason the many parts of the HERMES experiment providing and measuring the polarization of the target and the beam will not be described.

3.1 The HERA storage ring

The HERMES experiment runs at the storage ring HERA (Hadron-Elektron-Ring-Anlage) at the DESY (Deutsches Elektronen-Synchrotron) laboratory in Hamburg. The ring has a circumference of 6.3 km. Two beams are accelerated at HERA in opposite directions, a 920 GeV proton beam and a 27.5 GeV positron or electron beam [1].

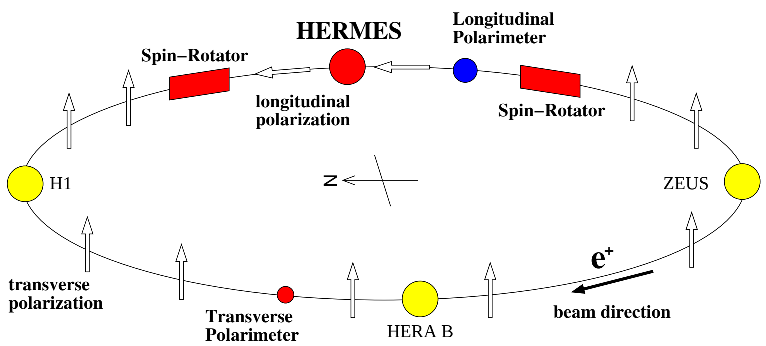

Figure 3.1: Sketch of the HERA positron ring at DESY in Hamburg, Germany. The open arrows indicate the direction of the beam polarization.

HERA hosts the four experiments H1, ZEUS, HERMES and HERA-B. Zeus

[1] In the present analysis only the positron beam was used. For that reason hereafter I'll only refer to a positron beam, but statements involving the positron beam apply also to an electron beam.

and H1 are colliding-beam experiments and Hera-B is a fixed-target experiment that uses the proton beam. The HERMES experiment is located at the east-hall of HERA (Fig. 3.1). It is a fixed-target experiment that uses the positron beam.

As was mentioned already, HERA normally provides a 27.5 GeV beam. However, in the fall of 2000 it has operated for a short period with a 12 GeV beam and the analysis presented in this thesis is specifically about the data taken at that energy.

3.2 The Spectrometer

The HERMES spectrometer consists of two identically constructed parts, one above and one below the positron beam pipe, as one can see in Fig. 3.2. In order to perform a semi-inclusive analysis, there are some characteristics of the scattering process that the spectrometer has to determine. It has to determine the angle[2] and momentum of the outgoing particles, the type of particles and it must also determine if the detected particles originate from the same scattering event. In this section the basics of the detectors involved will be discussed briefly (see [2] for a thorough description).

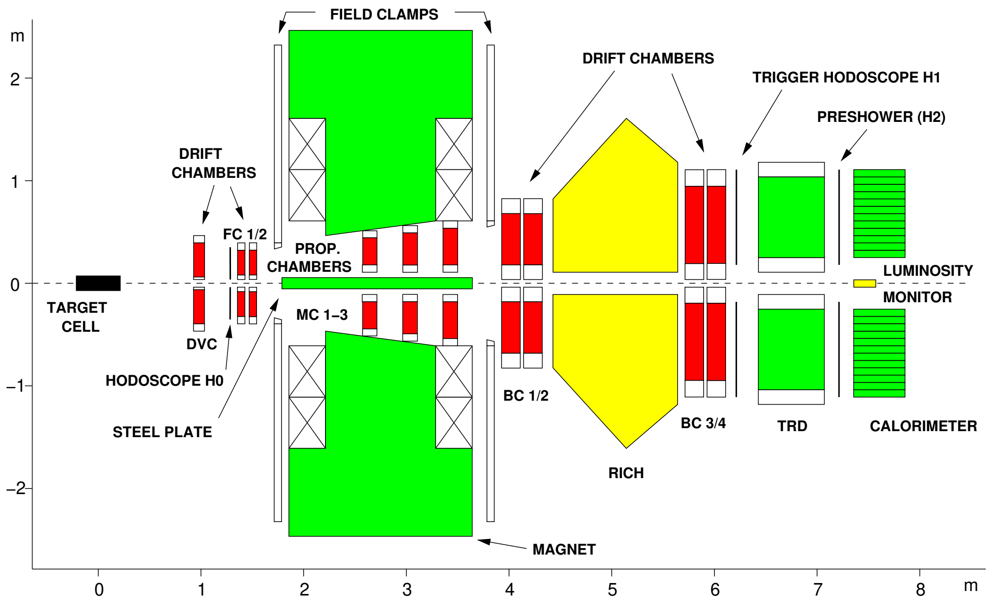

Figure 3.2: Schematic side view of the HERMES spectrometer

3.2.1 The Magnet

The HERMES spectrometer magnet deflects charged particles in order to determine their momentum. The gap between the pole faces encloses the geometrical

[2]The scattering angle for the positrons and the 'production angle' for the produced hadrons.

acceptance of 40 mrad $< |\theta_x| <$ 140 mrad vertically and $|\theta_y| <$ 170 mrad horizontally. As can be seen in Fig. 3.2, the pole faces are tilted parallel to the limits of the vertical angular acceptance. The positron and proton beam are shielded from the magnetic field by a steel plate, as indicated in the figure.

3.2.2 Tracking Detectors

The HERMES spectrometer contains several tracking detectors. A tracking detector measures the position of a charged particle where it went through the detector. Several of these detectors combined are used to reconstruct particle tracks.

The most important tasks of the tracking detectors in combination with a track reconstruction code are:

- Vertex reconstruction. The vertex is the position where the scattering event took place. The reconstructed vertex should lie in the target area. Also, the reconstructed vertex should be the same for primary particles originating from the same scattering event.

- Determination of the direction in which particles move (before they are deflected by the magnet).

- Determination of the momentum of the (charged) particles from the deflection in the spectrometer magnet.

Two types of tracking detectors are used, drift chambers (DVC, FC 1/2, BC 1/2, BC 3/4) and proportional chambers (MC 1/2/3). Their position in the spectrometer is shown in Fig. 3.2.

A multi-wire proportional chamber consists of a set of thin, equally spaced anode wires placed in the middle of two cathode planes. The space between the cathode planes is filled with a gas. A particle traversing the chamber can ionize the gas and the applied electric field will cause the electrons to drift towards an anode wire, causing an avalanche near the wire. This results in a current signal revealing the position of the particle (a better position resolution is obtained by interpolating between the signals of several sets of wires with different orientations).

A drift chamber is a multi-wire chamber in which spatial resolution is achieved by measuring the time electrons need to reach the anode wire, measured from the moment that the ionizing particle traversed the detector. This results in a higher resolution than can be obtained with multi-wire proportional chambers [6].

3.2.3 Particle Identification Detectors

In the HERMES spectrometer four detectors are used for particle identification, a Ring Imaging Čerenkov Counter (RICH), a transition-radiation detector (TRD), a pre-shower counter (H2) and a lead-glass calorimeter. The TRD, pre-shower and calorimeter are used to separate leptons and hadrons. The RICH is used to determine the hadron type. It is able to distinguish between pions, kaons and (anti)protons. In this section the basics of these four detector are discussed.

The pre-shower and the calorimeter both use the same principle to separate hadrons and positrons. Hadrons traversing detector material mostly loose their energy through inelastic collisions with the atoms of this material. They cause excitations and ionizations of the atoms in the detector material. Positrons, on the contrary, loose most of their energy through the radiation of *bremsstrahlung*, which results in an electromagnetic shower. Through this process, leptons are able to loose energy much faster in the detector material than hadrons, providing the possibility to separate them.

The pre-shower counter consists of a hodoscope (H2) with, in front of it, an 11 mm thick lead plate (2 radiation lenghts[3]) sandwiched between two 1.3 mm steel plates. The hodoscope consists of 42 vertical scintillator modules. Positrons deposit about $20 - 40$ MeV in the pre-shower counter, while pions deposit only about 2 MeV.

The calorimeter is composed of two walls, one above and one below the beam, of 420 identical lead-glass blocks, stacked in a 42×10 array. Each block has an area of 9×9 cm^2 and a length of 50 cm. Positrons loose almost all their energy in the 50 centimeters of lead-glas composite (18 rad. lenghts) of the calorimeter. Positrons and hadrons are separated using the particle distribution versus E/p. Here, E is the deposited energy and p the momentum of the particles. Positrons then appear as a sharp peak around $E/p = 1$, while the hadron peak shows up at a much lower value of E/p and is smeared out.

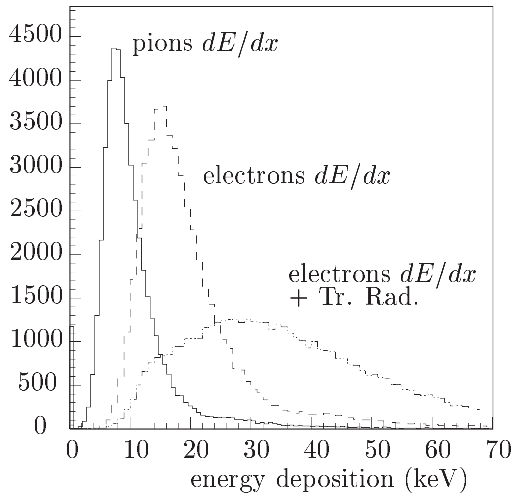

Figure 3.3: Response of a single TRD module for electrons and pions with an energy of 5 GeV [9]. The positron peak is shown with and without transition radiation. Monte Carlo simulation.

The TRD measures the electromagnetic radiation (X-ray) emitted by highly

[3]The radiation length is defined as the distance over which the energy of an electron is reduced by a factor $1/e$ due to radiation loss.

relativistic charged particles (Lorentz factor $\gamma > 1000$) that cross a boundary between two dielectric media (see for example [14]). The radiated energy is proportional to the Lorentz factor of the radiating particles. This offers the possibility of hadron-lepton separation, since leptons a much higher Lorentz factor as compared with hadrons at the same energy. For example, positrons with an energy of 5 GeV have a γ of order 10^4, whereas pions have $\gamma \approx 36$ at the same energy. In the HERMES energy regime, transition radiation is only produced by positrons, not by hadrons.

The radiation is emitted at a very small angle $\theta \sim 1/\gamma$ and therefore it is not possible to separate the transition radiation from other processes by which the positron looses energy in the detector (mostly Bremsstrahlung). A typical response of the TRD for one module (for a 27 GeV electron beam) is shown in Fig. 3.3.

Only a very small number of photons is radiated if a positron crosses a boundary. Therefore, a TRD constists of several layers in order to make the transition radiation detectable. The HERMES TRD consists of 6 modules above and below the beam. Each module contains a radiator and proportional wire chamber, optimized to detect X-ray photons. One radiator is 6.35 cm thick and consists on average of 267 dielectric layers.

When a charged particle traverses a dielectric medium it will radiate Čerenkov radiation if its velocity is higher than the speed of light in this material [19] (the so-called radiator), i.e. $v > \frac{c}{n}$ with n the refractive index of the material used. The RICH measures the opening angle of the cone of Čerenkov radiation, which is used to determine the velocity of the radiating particle. The opening angle is given by $\cos\theta_c = c/nv$.

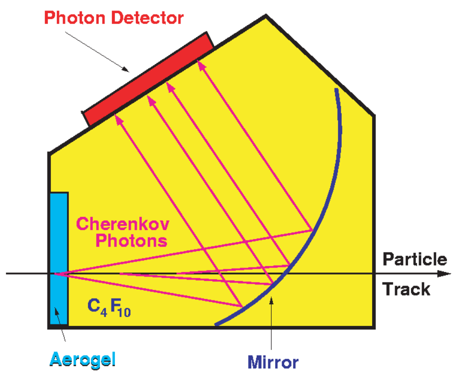

Figure 3.4: Schematic side view of the RICH

Combined with the momentum of the particle (given by the deflection of its path by the magnet) the velecity measurement yields the mass of the particle. The RICH at HERMES is a dual-radiator, meaning that a particle traverses *two* radiators, containing as radiators a wall of silica aerogel tiles and a volume of C_4F_{10}, a heavy fluorocarbon gas. As shown in Fig. 3.4 the Čerenkov cones are focussed by a spherical mirror onto a grid of photomultipliers, where they produce two concentric rings. The radius of a ring is proportional to the Čerenkov angle. Combined, the two radiators cover the momentum range from 2 GeV/c to 15 GeV/c.

3.3 PID scheme

As was discussed in the previous section, the calorimeter, pre-shower and the TRD are all used to separate hadrons and leptons. The measurements of these detectors are combined in order to obtain an optimal separation.

First, a PID'_s (Particle ID) value is constructed for all three detectors separately. For every track in the detector, depending on its energy and momentum, it gives the *logarithmic likelihood* that this track corresponds to a lepton or a hadron. It is given by

$$PID'_s = \log_{10} \frac{P(H_{\mathrm{l}}|E,p)}{P(H_{\mathrm{h}}|E,p)} \ , \tag{3.1}$$

where $P(H_{\mathrm{l(h)}}|E,p)$ is the probability that a particle with momentum p and an energy deposition in the detector E is a lepton or a hadron ($P(H_{\mathrm{l}}|E,p) + P(H_{\mathrm{h}}|E,p) = 1$). Using Bayes' theorem[4] this can be rewritten as:

$$PID'_s = \log_{10} \frac{P(E|H_{\mathrm{l}},p)P(H_{\mathrm{l}}|p)}{P(E|H_{\mathrm{h}},p)P(H_{\mathrm{h}}|p)} = PID - \log_{10}\Phi \ , \tag{3.2}$$

where

$$PID \equiv \log_{10} \frac{P(E|H_{\mathrm{l}},p)}{P(E|H_{\mathrm{h}},p)} \quad \text{and} \quad \Phi \equiv \frac{\phi_{\mathrm{h}}}{\phi_{\mathrm{l}}} = \frac{P(H_{\mathrm{h}}|p)}{P(H_{\mathrm{l}}|p)}. \tag{3.3}$$

In these equations $P(E|H_{\mathrm{l(h)}},p)$ is the probability that a lepton (hadron) with momentum p will deposit an energy E in the detector and $P(H_{\mathrm{l(h)}}|p)$ is the probability that a track with momentum p is a lepton (hadron). The variable $\phi_{\mathrm{l(h)}}$ represents the lepton (hadron) flux. For this reason the ratio Φ is called the *flux factor*.

For each track the value of $P(E|H_{\mathrm{l(h)}},p)$ is extracted from the *parent distribution*. The parent distribution gives the probability $P(E|H_{\mathrm{l(h)}},p)$ as a function of the deposited energy E for a certain momentum range. An example of a parent distribution is given in Fig. 3.5. The parent distribution can be obtained for each detector by selecting those tracks in the remaining PID detectors that correspond with high certainty to either a lepton or a hadron. The size of the momentum bins, and thus the width of the distributions, is chosen on account of the momentum resolution of the detector and the amount of statistics.

The flux factor is calculated through an iterative procedure. Since the particle fluxes depend on the momentum p of the particles and the polar angle θ of their tracks, the flux factor is evaluated in bins of these variables. First it is asumed that $\Phi(p,\theta) = 1$, corresponding to equal hadron and lepton fluxes. With this flux factor the PID' distribution is calculated (using Eq. (3.1)).

[4](see [15] or [28] for a detailed discussion)

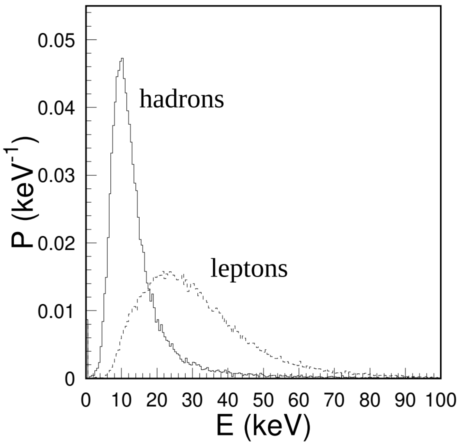

Figure 3.5: Parent distributions for module 1 of the TRD. The solid (dashed) curve shows the distribution for hadrons (leptons) in the momentum range $6-9$ GeV ($2-3$ GeV). Real data is shown, taken using a 12 GeV positron beam.

From this PID' distribution a new value for the flux factor can be calculated as:

$$\Phi_{new} = \frac{\#\text{ tracks with } PID' < 0}{\#\text{ tracks with } PID' > 0}, \tag{3.4}$$

wich gives a new PID' distribution. This procedure is iterated until convergence is reached.

After the PID distributions of all three detectors separately have been computed, they are combined in order to obtain the optimal lepton/hadron separation. The following PID' has been defined:

$$PID' = PID2 + PID5 - \log_{10}\Phi, \tag{3.5}$$

where

$$\begin{aligned} PID2 &\equiv PID_{\text{calorimeter}} + PID_{\text{pre-shower}} \\ PID5 &\equiv PID_{\text{TRD}}. \end{aligned}$$

A typical PID distribution is shown in Fig. 3.6, both with and without the flux factor correction. Here $PID2$ and $PID5$ are added[5]. Leptons can be selected by requiring $PID2 + PID5 > 0$. Though the shapes of the two curves are very different from each other, by using this selection the influence of the flux factor is rather small (the number of particles is given by the surface area under the curve).

[5]PID2 and PID5 are defined separately for historical reasons.

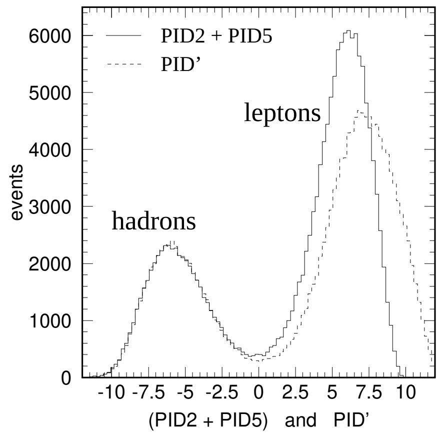

Figure 3.6: PID distribution with (dashed curve) and without (solid curve) the flux factor included for a sample of the ^{84}Kr data.

3.4 The luminosity monitor

The luminosity of a scattering process is defined as:

$$\mathcal{L} = I\rho/e, \tag{3.6}$$

with I the beam current, ρ the target density and e the positron charge.

The luminosity is an essential parameter needed to determine cross sections. It is related to the cross section σ as:

$$\sigma \sim R/\mathcal{L}, \tag{3.7}$$

with R the measured scattering rate.

The luminosity monitor provides an indirect measurement of the target density. This works in the following way: some of the beam positrons scatter elastically off the target gas electrons (Bhabba scattering, $e^+e^- \rightarrow e^+e^-$) and some of the beam positrons annihilate with the electrons into photon pairs ($e^+e^- \rightarrow \gamma\gamma$). The resulting particle-pairs are measured in the luminosity monitor. Since the cross sections for these processes are known very precisely, this gives a measure of the luminosity. The luminosity monitor consists of two small calorimeters as shown in Fig. 3.7.

It is situated at 7.2 m from the target cell. For a 12 GeV beam energy, the scattering angle of the scattered particle-pairs is smaller than for a 27 GeV beam. As a consequence the scattered particles are not detected in the luminosity monitor. Therefore, the luminosity monitor can not be used to extract cross sections when HERA is operated with a 12 GeV beam. For a 12 GeV beam energy cross sections can be obtained by normalizing to data from other experiments. The way this is done for the present analysis is discussed in section 4.3.

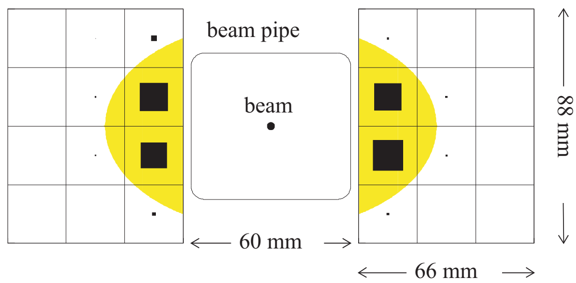

Figure 3.7: Hit distribution in the calorimeters of the luminosity monitor. The size of the boxes is proportional to the number of hits per channel. The shaded area shows the beam pipe acceptance [2]

Chapter 4

Analysis and results

Introduction

The hadron attenuation ratio has been studied for all charged hadrons together as well as for charged pions separately on nitrogen and krypton targets. The dependence of the attenuation ratio on the particle type has been investigated as well as the dependence on the charge of the hadrons. The A dependence of the data is also addressed.

A certain number of selections have to be applied to the data in order to obtain a clean sample of DIS events. These selections are the subject of section 4.1. When these selections have been applied, the data has to be corrected for radiative processes, which are treated in section 4.2. In section 4.3 it is explained how the attenuation ratio is extracted from the measurements. After that, section 4.4 describes the determination of the statistical and systematic uncertainties, and finally the results of the analysis are presented in section 4.5.

4.1 Data selection

4.1.1 Data quality

The Data AcQuisition system (DAQ) stores data into data blocks of 560 Mbytes, called runs. Each run is again divided into periods of 10 seconds, called bursts. To each burst corresponds a list of information on the detector performance. Data quality selections are applied at the level of runs, bursts and at the level of individual events. In the following list, those selections are explained that have been applied specifically in this analysis[1].

Selections at the level of runs:

- Runs are rejected whenever equipment malfunctioning is reported in the logbook (`g1Quality.iExpment`).
- The first and last burst in a run are removed, since they are not handled correctly by the DAQ (`g1Quality.iuDSTbad`).

[1] The corresponding fields in the data tables are shown between brackets.

Selections at the level of bursts:

- The TRD has to work properly for the top and the bottom detector (`g1Quality.iTrdDQ`).
- burst length < 11 s (`glDAQ.rLength`).
- DAQ (Data AcQuisition) dead time $< 20\%$ (`g1DAQ.rDeadCorr`).
- A burst is removed if there are dead blocks measured by the GMS (Gain Monitoring System) in the top or bottom calorimeter or in the pre-shower detector (`g1Quality.bCaloDead, g1Quality.bH2LumiDead`).
- Bursts with high-voltage trips in tracking detectors are removed (`glHVtrip`).

Selections at the event level:

- An event has to contain one track that is detected in all three hodoscopes and the calorimeter. The energy deposited in the calorimeter has to be $E_{calo} > 1.5$ GeV (`trigger 21`, `smTrack.bTrigMask`).
- A track is accepted if its azimuthal angle θ is contained within the geometrical acceptance of the detector:

  (i) 0.04 rad $< |\theta_y| <$ 0.14 rad,

  (ii) $|\theta_x| <$ 0.17 rad,

  where θ_y and θ_x are the projections of θ on the vertical and horizontal axis, respectively. The geometrical acceptance is determined by the size of the shielding plate and the calorimeter (see Fig. 3.2).
- The reconstructed vertex position has to lie within the target cell:

  (i) -18.0 cm $< z_{\text{vertex}} <$ 18.0 cm

  (ii) $|t_{\text{vertex}}| <$ 0.75 cm.

  Here z_{vertex} is the position in the target cell along the beam and $|t_{\text{vertex}}|$ is the (transverse) distance of the reconstructed vertex from the z-axis (axis along the beam pipe).

4.1.2 Particle Identification

In Fig. 4.1 the PID' distributions are shown for all three targets for a sample of the data. Leptons and hadrons are selected from the data by applying the following cuts:

$$\text{leptons}: \quad PID' > 1 \tag{4.1}$$

$$\text{hadrons}: \quad PID' < 0 \tag{4.2}$$

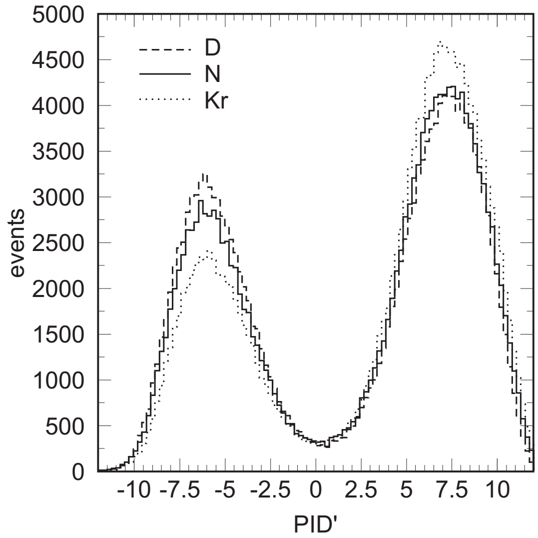

Figure 4.1: The PID' distributions for a subsample of the data for krypton (dotted curve), nitrogen (solid curve) and deuterium (dashed curve).

These PID' cuts are chosen to combine a high *efficiency* and a low *contamination*. Expressions to calculate the efficiency of the lepton selection and the hadron contamination into the lepton sample are given respectively by:

$$\epsilon = \frac{\displaystyle\int_{PID'_{cut}}^{\infty} dPID'\ P^l\ N}{\displaystyle\int_{-\infty}^{\infty} dPID'\ P^l\ N} \qquad \text{and} \qquad h = \frac{\displaystyle\int_{PID'_{cut}}^{\infty} dPID'\ P^h\ N}{\displaystyle\int_{PID'_{cut}}^{\infty} dPID'\ N}, \tag{4.3}$$

where $P^l = P(H_l|E,p)$ and $P^h = P(H_h|E,p)$ (see Eq. (3.1)). The results are listed in table 4.1. Using expressions similar to 4.3 the efficiency of the hadron selection and the contamination of leptons into the hadron sample can be obtained. The values of ϵ and h for the cut $PID' < 0$ are given in table 4.2.

	krypton	nitrogen	deuterium
Efficiency	98.8%	98.5%	98.7%
Contamination	0.1%	0.1%	0.1%

Table 4.1: Lepton efficiency and hadron contamination for the lepton selection $PID' > 1$.

The pion identification is performed by using information of the RICH detector. For each hadron the RICH software provides the probability that this hadron is a pion, a kaon or a proton. Pions are selected if the probability for a hadron to correspond to a pion is higher than 50%.

	krypton	nitrogen	deuterium
Efficiency	99.2%	99.3%	99.5%
Contamination	0.8%	0.7%	0.6%

Table 4.2: Hadron efficiency and lepton contamination for the hadron selection $PID' < 0$.

4.1.3 Kinematics

Only part of the data that passed the data-quality selections consists of DIS events. Inclusive DIS events are selected by the following cuts:

$$Q^2 > 0.5 \text{ GeV}^2 \tag{4.4}$$
$$W^2 > 4 \text{ GeV}^2 \tag{4.5}$$

With the constraint on Q^2 events are selected outside of the region where scaling violations are observed. Usually this cut is chosen within 0.2 and 1 GeV^2. Here 0.5 GeV^2 is chosen (and not a more conservative cut $Q^2 > 1$ GeV^2), because a large fraction of the total number of events lie within the region $0.5 < Q^2 < 1$ GeV^2 ($\approx 69\%$). The requirement on the invariant mass $W^2 > 4$ excludes events from the resonance region. For events where the scattered positron has a low momentum, there is a large contribution of background processes. They are excluded by the following constraint on the positron energy:

$$E' > 2.5 \text{ GeV}. \tag{4.6}$$

Fig. 4.2 shows the kinematic distribution (Q^2 versus ν) of the scattered

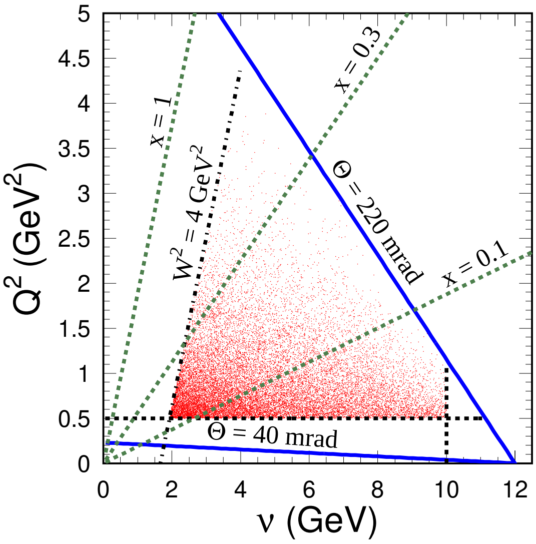

Figure 4.2: Kinematic distribution of the inclusive DIS events as a function of Q^2 and ν. The applied constraints on W^2, Q^2, ν and θ are indicated by the lines.

positrons after the kinematical selections have been applied. The selections are indicated by lines in the figure. Lines for some values of x-bjorken are also included in the figure. Events at $x = 1$ would correspond to elastic scattering.

Semi-inclusive events are selected from the inclusive ones by demanding at least one hadron to be identified per event. For hadrons it is then additionally required that:

(i) $z > 0.2$,

(ii) $p_h > 1$ GeV or $p_\pi > 2.5$ GeV,

where p_h and p_π are the hadron and pion momentum, respectively. The large pion momentum cut is due to the RICH momentum threshold for pions. With the requirements $z > 0.2$ and $p_h > 1$ GeV, hadrons are selected with large forward momentum to ensure they are originating from current fragmentation or central fragmentation. Using this selection, the hadron sample will consist mostly of *leading* hadrons (i.e. hadrons containing the struck quark).

As a result of the energy cut for hadrons/pions (i,ii), the kinematic range covered in ν will depend on the value of z and vice versa, as is indicated in Fig. 4.3.

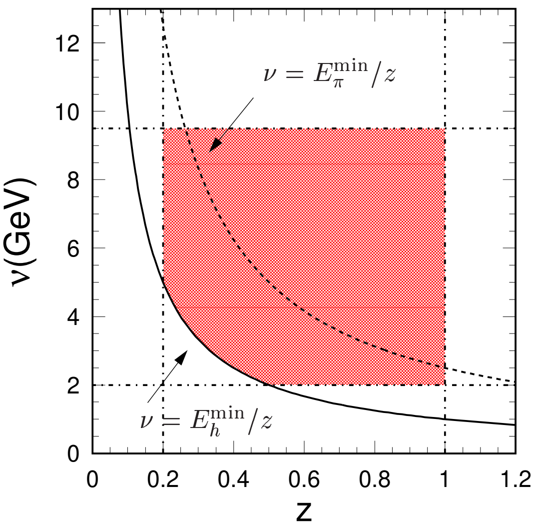

Figure 4.3: Influence of the hadron/pion energy selection on the kinematic range covered by the data in ν and z. The solid (dashed) curve shows the lower ν value for all hadrons (pions). The kinematic range covered for all hadrons (pions) is indicated by the gray area. The applied selections on z and ν are also indicated ($z > 0.2$, $\nu < 9.5$ GeV).

The total number of events remaining, after all the constraints have been applied, is given in Table 4.3.

	krypton	nitrogen	deuterium
# DIS	600596	589734	718408
# hadrons	39150	50465	69149
# pions	13819	20462	28577

Table 4.3: Total number of inclusive and semi-inclusive events. Note that different selections have been applied to the hadron sample than to the pion sample.

4.2 Radiative Corrections

The measured cross section has to be corrected for radiative processes in order to obtain the Born cross section, corresponding to the process depicted in Fig. 4.4. The most important radiative processes are represented by the Feynman diagrams of Fig. 4.5. The diagrams in Fig. 4.5(a) and 4.5(b) are second-order

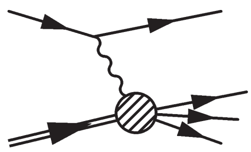

Figure 4.4: Lowest order DIS process.

QED corrections for final-state and initial-state Bremsstrahlung, respectively. Fig. 4.5(c) and 4.5(d) are second-order corrections to the lepton-photon vertex. Besides these radiative DIS processes, also a contribution from the radiative tail of non-DIS processes (i.e. elastic, quasi-elastic) has to be taken into account.

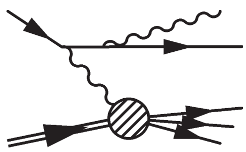

(a) final-state radiation

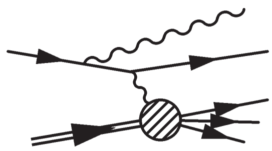

(b) initial-state radiation

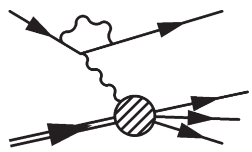

(c) Schwinger correction

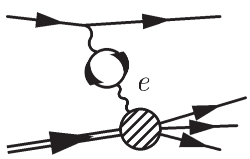

(d) vacuum-polarization correction

Figure 4.5: Most important DIS processes contributing to the radiative corrections.

The correction factors are calculated by the program TERAD [27], which uses the values of x and y as input. In the extraction of the attenuation ratio, radiative corrections need to be applied both to the semi-inclusive DIS cross section ratio and to the inclusive DIS cross section ratio (Eq. (2.7)). They have been applied according to the following expressions.

For the inclusive ratio:

$$\frac{\sigma_A^{\rm DIS}}{\sigma_D^{\rm DIS}} = \frac{1}{\eta_D^{\rm DIS}} \left[\frac{\sigma_A^{\rm DIS}}{\sigma_D^{\rm DIS}}\right]_{\rm meas} - \frac{\sigma_A^{\rm bg}}{\sigma_D^{\rm DIS}}, \tag{4.7}$$

where $\eta_D^{\rm DIS} = 1/(1+\sigma_D^{\rm bg}/100)$ and $\sigma^{\rm bg}$ indicates the (background) cross section including *all* radiative processes (quasi-elastic,elastic, inelastic etc.), where $\sigma^{\rm bg}$ is given as a fraction of the Born cross section.

For the semi-inclusive ratio:

$$\frac{\sigma_A^{\rm SIDIS}}{\sigma_D^{\rm SIDIS}} = \frac{\eta_A^{\rm inel}}{\eta_D^{\rm inel}} \left[\frac{\sigma_A^{\rm SIDIS}}{\sigma_D^{\rm SIDIS}}\right]_{\rm meas}. \tag{4.8}$$

In this equation $\eta^{\rm inel} = 1/(1+\sigma^{\rm inel}/100)$ is calculated using only the contribution of inelastic radiative processes to the background cross section. In the case of semi-inclusive scattering, there is no contribution of elastic or quasi-elastic radiative processes, since at least one hadron is detected in coincidence with the scattered lepton.

A thorough discussion of the method used in Eqs. 4.7 and 4.8 to apply the radiative corrections is given in [3].

4.3 Attenuation ratio

In the previous section it was shown that radiative corrections have to be applied to the measured cross section ratios (Eq. (4.7) and Eq. (4.8)). In the experiment the number of inclusive events and the number of semi-inclusive hadrons is measured, resulting in measured yield ratios. However, to extract a cross section ratio from a yield ratio, the luminosity has to be known, which is not available for the 12 GeV data (as discussed in sec. 3.4). Therefore, the measured yield ratio is normalized to NMC data in the region $0.1 < x_{\rm bj} < 0.4$,

$$\left[\frac{\sigma_A^{\rm DIS}}{\sigma_D^{\rm DIS}}\right]_{\rm meas} = X \, \frac{N_e^A}{N_e^D}, \tag{4.9}$$

where X is the normalization factor (1.223 for ^{84}Kr, 1.234 for ^{14}N) and N_e^A (N_e^D) are the number of measured inclusive events for target A (^{2}H).

The same factor is applied to the measured yield ratio of semi-inclusive hadrons. Note that due to the subtractive term in Eq. (4.8) these two normalization factors do not cancel.

4.4 Error calculation

4.4.1 Statistical uncertainty

The number of semi-inclusive events is a subset of the number of DIS events. The hadron multiplicity per semi-inclusive event is approximately equal to one (on average ~ 1.01). Therefore, it is possible to calculate the statistical error to the numerator and to the denominator of the attenuation ratio (see Eq. (2.7)) using the binomial theorem [25]:

$$\Delta\left[\frac{N_h^A(z,\nu)}{N_e^A(\nu)}\right] = \frac{N_h^A(z,\nu)}{N_e^A(\nu)}\sqrt{\frac{1}{N_h^A(z,\nu)} - \frac{1}{N_e^A(\nu)}}. \tag{4.10}$$

Since the number of events for different targets is statistically independent, the statistical uncertainty on the attenuation ratio can then be derived by conventional error propagation.

4.4.2 Systematic uncertainty

Most of the systematic uncertainties largely cancel, since the attenuation is evaluated as a ratio of cross section ratios (Eq. (2.7)). Dominant sources of systematic uncertainties are the radiative corrections and diffractive ρ^0 production. The systematic uncertainty due to the radiative corrections is 2%. This number is taken from a comparison to the analysis of the inclusive cross section ratio for the 12 GeV data [31]. In the calculation of the radiative corrections, it has not been taken into account that the corrections for the *semi-inclusive* cross section ratio depend on z. This dependence is accounted for by an additional 3% error in the systematic uncertainties (see [30]).

In diffractive ρ^0 production the virtual photon fluctuates into a virtual $q\bar{q}$-pair, which can produce a real ρ^0 by interaction with the nucleus. The produced ρ^0 will decay with a branching ratio of $\approx 100\%$ into a $\pi^+\pi^-$ pair. The process of diffractive ρ^0 production contributes to the measured DIS samples. For the 27 GeV data[2] the influence of diffractive ρ^0 production on the attenuation ratio has been studied and it was estimated to give a 1.5% contribution to the systematic uncertainties [12]. Exclusive ρ^0 production has been studied for the 12 GeV data and for the 27 GeV data [26] and the contribution of ρ^0 production in the DIS sample was measured to be approximately equal for both data sets. Therefore, also a 1.5% contribution to the systematic uncertainties is used for the 12 GeV data.

The uncertainties of the radiative correction and diffractive ρ^0 production combined give a total systematic uncertainty of 3.9%.

Other sources of systematic uncertainties like charge symmetric background processes and a dependence of the attenuation on the detector acceptance as well as an uncertainty due to the NMC normalization (Eq. (4.9)) are negligible and are not taken into account in the present analysis.

[2] A similar analysis of the hadron attenuation as been done at HERMES using a 27 GeV positron beam energy. This will be discussed in sec. 4.5.1

4.5 Results

In this section the results of the analysis are presented. All plots in this secion include only the *statistical* uncertainty, the systematic uncertainty adds an overall 3.9% to the uncertainty (see sec. 4.4).

The result for the charged hadron attenuation for both targets, ^{14}N and ^{84}Kr, as a function of ν, is shown in Fig. 4.6. Both targets show a significant attenuation in the whole ν range and it is much larger for the krypton target than for the nitrogen target. This confirms that the hadron formation process is influenced by the nuclear environment and that it depends on the atomic number A. Both targets show a decrease of the attenuation going to higher

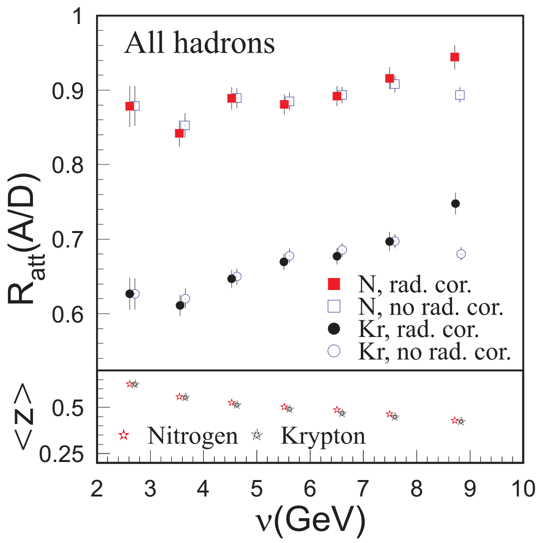

Figure 4.6: Hadron attenuation for krypton and nitrogen versus ν (upper panel). The full (open) symbols give the ratio with (without) radiative corrections. In the lower panel the average z is shown for all ν bins. Here positive and negative hadrons are combined. In both panels, points are shifted in ν in order to be able to distinguish overlapping points.

values of ν. This might reflect the fact that for high ν a larger fraction of hadrons is formed outside of the nucleus.

To give an idea of the size of the radiative corrections, the figure includes the ratios without radiative corrections. Only in the last bin the contribution is relevant. This can be explained by the fact that the radiative corrections are largest for small x and large y. For increasing ν, the average value of x decreases and the average value of y increases, so indeed the largest corrections are expected for high ν.

For charged *pions*, the attenuation versus ν is given in Fig. 4.8. The ratio is given separately for positive and negative pions. Also for pions the attenuation is increasing at low ν. The overall attenuation is larger for pions than for all hadrons together. The curves in the figure show the result of the calculation of the rescaling model [1] and the flavor dependent model [4]. The models use the kinematics corresponding to the 12 GeV data except for the Q^2 range, both models use $Q^2 > 1$ GeV^2. This is justified by the fact that the attenuation ratio does not depend significantly on Q^2, as can be seen in Fig. 4.7.[3]

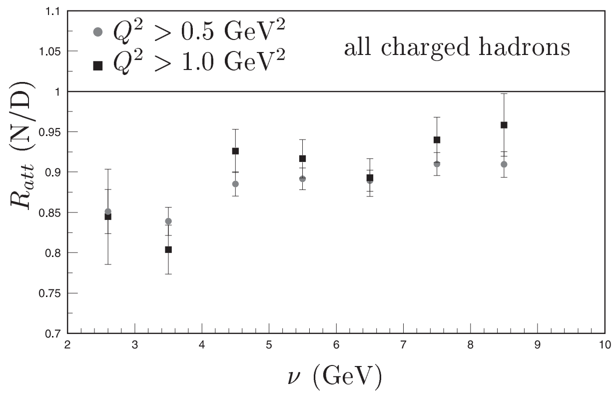

Figure 4.7: Hadron attenuation ratio for all charged hadrons as a function of ν for a ^{14}N target [18]. The result is shown with the constraint $Q^2 > 0.5$ GeV^2 and with the constraint $Q^2 > 1.0$ GeV^2

Neither model is able to describe the A dependence of the attenuation ratio, they both reproduce the data only for one of the targets. The flavor dependent model predicts a small charge dependence for the pion attenuation on the krypton target. However, within the uncertainty of the data such charge dependence can not be confirmed.

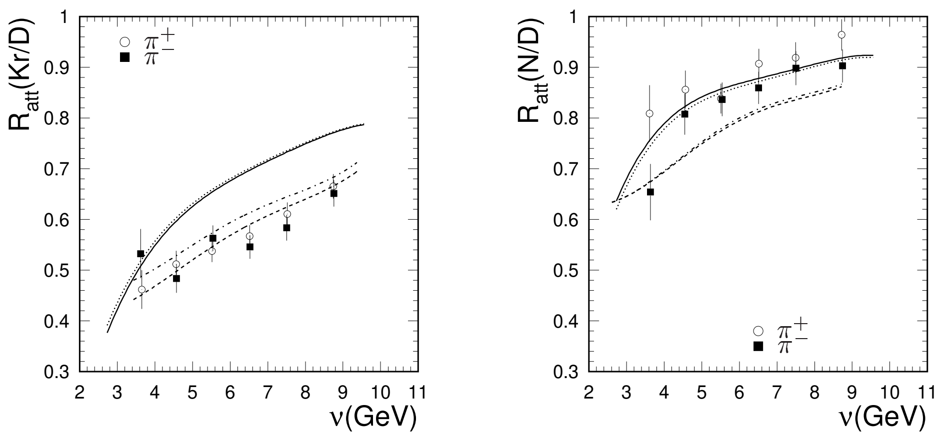

Figure 4.8: Attenuation ratio for positive and negative pions as a function of ν, for krypton (left) and for nitrogen (right). The solid (dotted) curve is the result of the rescaling model [1] calculation for positive (negative) pions. The dashed (dash-dotted) curve shows the flavor dependent model [4] calculation for positive (negative) pions.

[3]The figure shows results from an independent analysis of the attenuation ratio for a 12 GeV beam, done by the HERMES collaboration group from Bari, Italy. This will be discussed in more detail in sec. 4.5.2

In Fig. 4.9 the attenuation is shown as a function of z. The ratio is given separately for positive and negative hadrons. For both targets the attenuation increases with increasing z, although this behavior is much clearer for the krypton target (left plot) than for the nitrogen target (right plot).

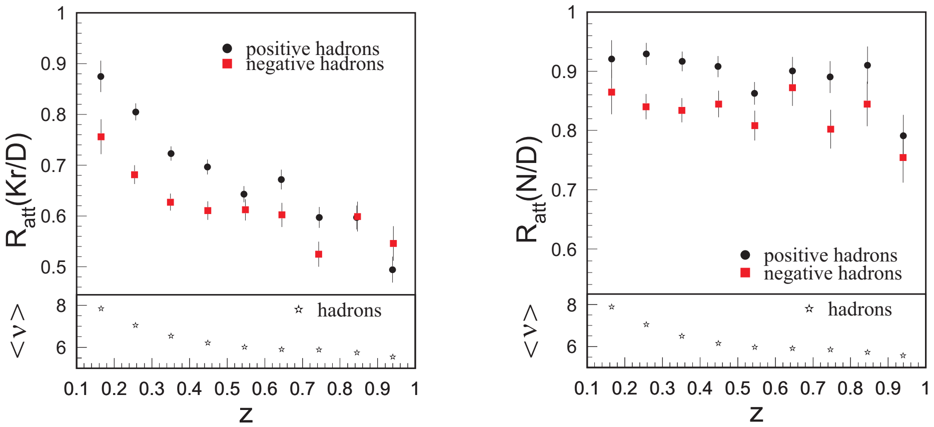

Figure 4.9: Attenuation ratio for positive and negative hadrons as a function of z, for krypton (left) and for nitrogen (right).

The observed z dependence might indicate that fast forward hadrons are formed well inside the nucleus. Model calculations for the attenuation ratio versus z are only available from the rescaling model for charged pions. The result is shown in Fig. 4.10. A string tension of $\kappa = 0.4$ GeV/fm has been used here, instead of the $\kappa = 0.25$ GeV/fm that was used for the calculation of the attenuation ratio for the kinematics of the 27 GeV data (see sec. 2.6). The model shows the same trend of the attenuation ratio versus z as the data. As mentioned before (section 2.6) the rescaling model attributes this behavior to a z dependence of the formation time, see Eq. (2.23). Using this equation it is concluded that hadrons with a high value of z will have shorter formation times.

Fig. 4.9 shows that the attenuation ratio for hadrons is charge dependent, whereas Fig. 4.10 for the *pion* attenuation shows no significant charge dependence of the attenuation ratio at all. Therefore, the charge dependence for the hadron sample must be due to other hadrons, like (anti)protons or kaons. However, it is expected that the attenuation of kaons is similar to that of pions and because of that it is not likely that the charge dependence is due to kaons.

Monte Carlo studies (for the 27 GeV data) showed that the amount of protons in the positive hadron sample (24%) is larger than the amount of antiprotons in the negative hadron sample (6%) [29]. A similar difference is expected for the 12 GeV data. Therefore, a possible explanation for the difference in attenuation is a larger formation time for protons than for pions. Here, it is assumed that kaons have a formation time comparable to pions.

Another possible explanation is a difference between the proton-nucleon cross section and the antiproton-nucleon cross section.

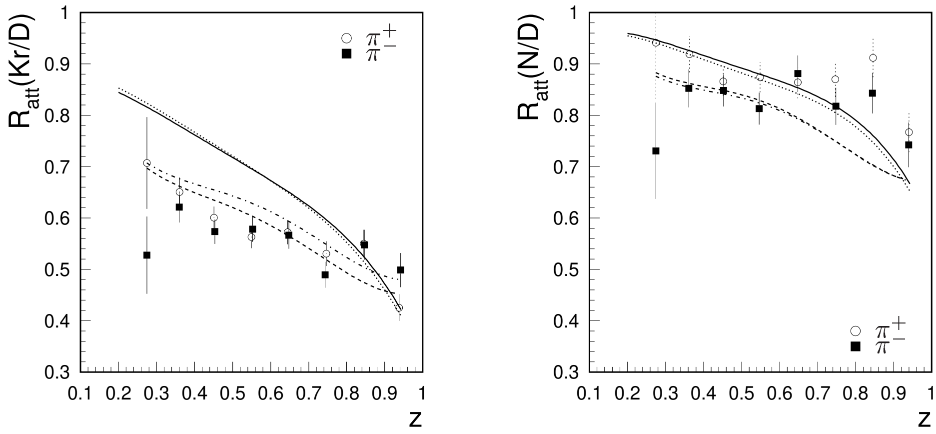

Figure 4.10: Attenuation ratio for positive and negative pions as a function of z, for krypton (left) and for nitrogen (right). The solid (dotted) curve is the result of the rescaling model [1] calculation for positive (negative) pions. The dashed (dash-dotted) curve shows the flavor dependent model [4] calculation for positive (negative) pions.

4.5.1 Comparison with 27 GeV analysis

A comparison is done with the 27 GeV analysis [30] for the attenuation ratio as a function of ν. By merging the results from both analyses the attenuation is obtained for a very broad range in ν (2.5 GeV to 22.5 GeV). The result is shown in Fig. 4.11

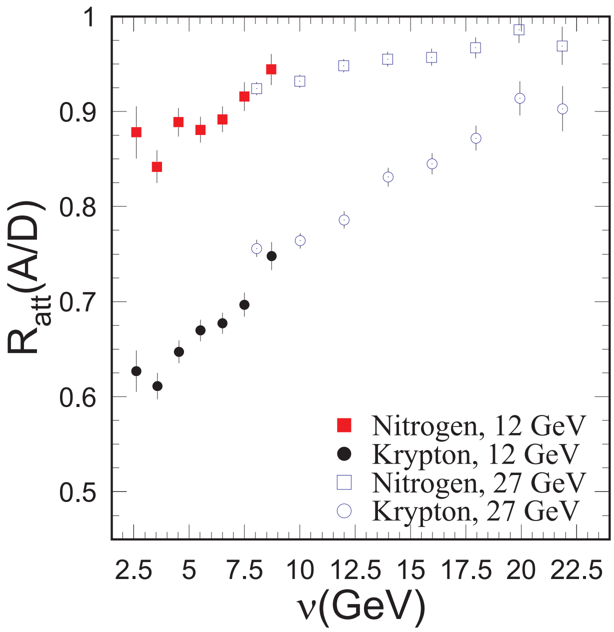

Figure 4.11: Attenuation ratio for all hadrons for the 12 GeV and the 27 GeV data as a function of ν.

The kinematical selections applied to the two analyses are the same except for the requirement on the lower limit of Q^2. For the 12 GeV analysis $Q^2 > 0.5$ GeV^2 and for the 27 GeV $Q^2 > 1$ GeV^2. However, the results can still be compared since the dependence of the attenuation ratio on Q^2 is small, as was shown in Fig. 4.7.

Fig. 4.12 shows the different (x,Q^2)-range covered by the 12 GeV data set as compared with the 27 GeV data set. Here, Q^2 is plotted versus ν. The boundaries are determined by the angular acceptance of the spectrometer and the cut $W^2 > 4$ GeV^2. Note that the constraint on Q^2 is not shown in this figure.

Important to note from this result is that the dependence on the atomic number A as observed in the present analysis agrees with that on the 27 GeV data. Also, a similar trend in the dependence of the attenuation ratio versus ν is observed, with a good agreement in the overlapping region at ν between 7.5 and 9 GeV.

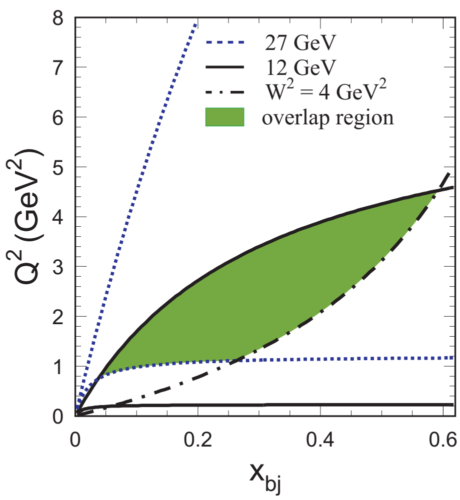

Figure 4.12: (x,Q^2)-range covered by the 12 GeV inclusive data compared to the 27 GeV data. The shaded area indicates the overlap region between the two data sets. The range shown in x is the range covered by the 12 GeV data, the 27 GeV data covers a larger region in x.

In Fig. 4.13 the attenuation ratio versus z for krypton is shown for the 27 GeV data and the 12 GeV data. The figure includes gluon-bremsstrahlung model [16] calculations for the kinematics of the 27 GeV data. Important to note is that the model calculation is valid for charged mesons only. However, since 80% of the hadron sample consists of pions (for the 27 GeV data) this can still give a fair comparison. Calculations of this model are not yet available for the kinematics of the 12 GeV data.

Although the kinematics is different, resulting in a stronger attenuation for the 12 GeV data, both data sets show a similar trend of the attenuation ratio versus z.

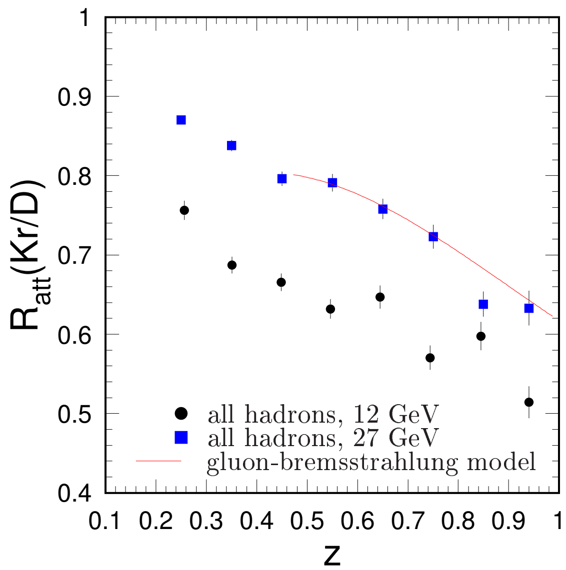

Figure 4.13: Hadron attenuation for krypton versus z for the 12 GeV data and the 27 GeV data. The curve shows the result from the gluon-bremsstrahlung model for the *meson* attenuation.

4.5.2 Analysis cross-check

An independent analysis, using a different code, has been performed by the HERMES collaboration group from Bari[4] [18]. The result on the attenuation ratio is shown for both targets, ^{14}N and ^{84}Kr, versus ν in Fig. 4.14. Radiative corrections have not been included here. Since both groups use the same program (TERADNMC) to calculate the radiative corrections this does not affect the comparison of the two analyses. The two analyses show a very good agreement, thus confirming the results presented in this thesis.

In principle the results should be exactly the same, because the same data selections (as discussed in section 4.1) have been applied. A small discrepancy might be due to a small difference in the total number of runs analyzed.

4.5.3 Formation time

From the model calculations available for the 12 GeV data presented in this section, it is not yet possible to conclude which model gives the best description of the data. Calculations still have to be done for the gluon-bremsstrahlung model and for the flavor dependent model for the attenuation ratio versus z. Therefore, it is not possible to give a definite answer on the value of the formation time for hadrons. However, it is possible to give an idea on the values

[4]University of Bari, Italy

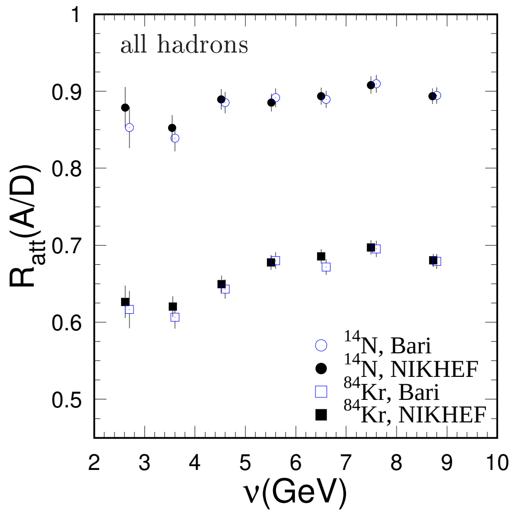

Figure 4.14: Cross-check between the Bari and the NIKHEF analysis. The attenuation ratio is plotted versus ν for krypton and nitrogen. No radiative corrections are applied for the comparison. The open symbols are shifted in ν in order to be able to distinguish overlapping points.

predicted by the gluon-bremsstrahlung model and the rescaling model, using Eq. (2.25) and Eq. (2.23). For the average ν (6.96 GeV) and z (0.60) of the krypton data the models predict the following formation time for pions:

- $1.2 \cdot 10^{-23}$ s (gluon-bremsstrahlung model)
- $2.1 \cdot 10^{-23}$ s (rescaling model)
- $9.4 \cdot 10^{-24}$ s (flavor dependent model)

The formation times given by the rescaling model and the flavor dependent model agree with the predictions of the attenuation ratio shown in Fig. 4.10 and 4.8. The flavor dependent model predicts for both targets an overall stronger attenuation, corresponding to a shorter formation time.

Chapter 5

Conclusions

The attenuation ratio has been studied on ^{14}N and ^{84}Kr as a function of ν and z using a 12 GeV positron beam. The objective was to get a better understanding of the hadronization process and specifically to obtain information on the formation time τ_h of the hadron. The observed attenuation is much larger for the ^{84}Kr target than for the ^{14}N target. This shows that the hadronization process is influenced by the nuclear environment. For both investigated targets the attenuation decreases as a function of ν, which could indicate that for high values of ν the final hadron is formed outside the nucleus.

For the ^{84}Kr target, the attenuation ratio is strongly z-dependent, showing a large increase of the attenuation with increasing z. For the ^{14}N target the z-dependence is less pronounced. The dependence on z might indicate that hadrons with a large value of z are formed very short after the hard virtual photon-quark interaction, leaving a relatively long time period for reinteractions within the nucleus.

The results of the models presented in this report reproduce the observed trend of the attenuation ratio versus z and ν. The rescaling model, the flavor dependent model as well as the gluon-bremsstrahlung model all attribute a large fraction of the attenuation to nuclear absorption, which again indicates that at high ν the final hadron is formed within the nucleus.

It is not possible yet to make any conclusive statements from the comparison with the model calculations stating which model better reproduces the data. Calculations from the rescaling model and the flavor dependent model are compared with the data for the attenuation ratio for charged pions for both targets. Neither model fits the data for both targets. From the gluon-bremsstrahlung model no calculation are available for the 12 GeV data yet. Therefore, at this moment no conclusion can be given on the values of hadron formation times. However, one thing that can be concluded is the way the formation time depends on z and ν. At high z all models that have been discussed predict

$$\tau_h \propto (1 - z)\nu,$$

which is in agreement with the measured z and ν dependence of the attenuation ratio.

In order to further investigate the hadron formation times the following studies can be done in the future:

- The RICH is able to identify pions with momentum $p_\pi > 2.5$ GeV. Most of the pions have momentum below this treshold. By adding particle identification by the time-of-flight method, the pion sample can be significantly enlarged.
- The attenuation ratio can be studied as a function of other variables then ν and z, like for instance Q^2 in order to be able to distinguish between different model predictions in a better way.
- The attenuation ratio can be studied for kaons and protons separately, as was done for the pions.

Acknowledgements

I would like to thank the following people for their support:

Most importantly I would like to thank Erika Garutti and Henk Blok for a lot of fruitful discussions and endless amounts of time. I learned a lot! Furthermore I would like to thank Luigi Lagamba, Beni Zihlmann, Gerard van der Steenhoven, Alberto Accardi, Grigozyan Levon, Vladas Tvaskis, Jos Steijger, Joost van Mameren en Bram van den Broek. You all helped me in one way or another to realize this master's thesis.

Bibliography

[1] A. Accardi, H.J. Pirner, *Nuclear modifications of fragmentation functions and rescaling models*, Talk presented at the 'European workshop on the QCD structure of the nucleon', Ferrara (ITA) (2002)

[2] HERMES collaboration, K. Ackerstaff et al., *The HERMES spectrometer*, Nucl. Instrum. Methods A **417**, 230 (1998)

[3] Note from Andy Miller: ∼`millera/public/Uradcorr.ps.gz`

[4] N.Z. Akopov, G.M. Elbakyan, L.A. Grigoryan, *Nuclear attenuation of charged mesons in deep inelastic scattering*, HERMES internal note 02-004 (2002)

[5] Comments Nucl. Part. Phys., Vol. **21**, No. 1, pp. 1-39 (1992)

[6] R. K. Bock, internet page <http://rkb.home.cern.ch/rkb>

[7] F.E. Close, *An Introduction to Quarks and Partons* (Academic Press, 1979)

[8] P.D.B. Collins and A.D. Martin, *Hadron Interactions* (Hilger Ltd, 1984)

[9] J.V. Emmerson, *Modeling of the HERMES TRD*, thesis, Simon Fraser University (1995)

[10] M.A.Funk, *A Measurement of the Polarised Parton Densities of the Nucleon in Deep-Inelastic Scattering at HERMES*, dissertation, Hamburg (1998)

[11] H.P.Blok, (E,E'X) reactions, in *Proceedings of the 13th Annual Hampton University Graduate Studies at CEBAF* (World Scientific, 1999)

[12] J.J.van Hunen, Deep-Inelastic Scattering off 14N, Ph.D. thesis, Utrecht University (2000)

[13] F. Halzen and A.D.Martin, *Quarks & Leptons* (J.Wiley & Sons, 1984)

[14] J.D. Jackson, *Classical electrodynamics* (J. Wiley & Sons, 1975)

[15] R. Kaiser, *Particle Identification at HERMES*, HERMES internal note 97-025 (1997)

[16] B.Z. Kopeliovich, J. Nemchik, E. Predazzi, *Hadronization in nuclear environments and electroproduction of leading hadrons* (hep-ph/9511214) (1995)

[17] B.Z. Kopeliovich, J. Nemchik, E. Predazzi, *Hadronization in nuclear environment* (nucl-th/9607036) (1996)

[18] L. Lagamba, private communications

[19] W.R. Leo, *Techniques for nuclear and particle physics experiments*, Springer-Verlag (1987)

[20] B. Ansersson, *The Lund Model* (Cambridge Univ. Press, 1998)

[21] J. van der Marel, thesis, Delft University (1997).

[22] F.M.Menden, *Measurement of the Valence Quark Spin Distributions of the Nucleon Using Deep Inelastic Scattering at HERMES*, thesis, Hamburg (1997)

[23] F.M.Menden, *Determination of the Gluon Polarization in the Nucleon*, dissertation, Hamburg (2001)

[24] A.A.Sokolov, I.M.Ternov, Sov. Phys. Dokl.8, 1203 (1964)

[25] J.J.M. Steijger, *Statistics critique*, HERMES (NIKHEF) internal note (2002)

[26] J.E. Sundermann, summer student report *Exclusive diffractive production of* ρ^0 *at* 12 *GeV and* 27 *GeV beam energy* (2001)

[27] I. Akushevich, A. Brüll and T. Shin, *Radiative corrections to the structure function ratio's*, HERMES internal note.

[28] J. Wendland, *Particle Identification for HERMES RUN I*, internal note 01-067 (2001)

[29] HERMES collaboration, A. Airaperian et al., *Hadron formation in deep-inelastic positron scattering in a nuclear environment* hep-ex/0012049 and Eur. Phys. Jour. **C** 20, 497-486 (2001)

[30] N.Bianchi, P.Di Nezza, E. Garutti, V. Muccifora, HERMES internal note 01-022 (2001)

[31] B. Zihlmann, private communications

[32] A. Bialas, M. Gyulassy, *Lund model and an outside-inside aspect of the inside-outside cascade*, Nucl. Phys. B**291** 793-812 (1987)

[33] D.H, Perkins, *Introduction to High Energy Physics* (Addison-Wesley publishing company, 1982)

[34] Particle Data Group, Review of particle physics, Phys. Rev. D, **54**(1) (1998)

Appendix A

A bit of QCD

One single quark is always surrounded by a cloud of virtual particles. A quark emits virtual gluons, which can fluctuate in virtual quark-antiquark pairs. This is the vacuum polarization of the color field. Vacuum polarization occurs for QCD as well as for QED. Also the electron is surrounded by a cloud of virtual particles, i.e. virtual photons, electrons and positrons. The interesting thing is that the result of this vacuum polarization is entirely different for QCD than for QED. In Fig. A.1 the lowest order Feynman diagrams are shown for the quark-antiquark interaction and for the electron-positron interaction. The lowest order corrections for the vacuum polarization are shown in Fig. A.2. For the electron-positron interaction this vacuum polarization correction results in a shielding of the 'bare' electron charge. As a consequence of this, the interaction will depend on Q^2. As was mentioned before, Q^2 gives a measure of the resolution with which a system is probed. In this case, by increasing Q^2, more and more of the 'bare' electron charge will be observed.[1] This behaviour is also seen in experiments. For example, the charge of the electron measured at CERN's LEP electron-positron collider yields the coupling constant $\alpha \approx 1/128.9$ [34], whereas low Q^2 experiments give the more familiar $1/137$ ($\alpha = e^2/4\pi\hbar c$). The electron-positron interaction can be calculated in pQED taking into account the vacuum polarization terms (using renormalization theory). The expansions calculated in pQED only converge for a coupling constant smaller than one (approximately). However, for the energies involved in present day experiments this is always true.

In QCD the coupling constant is also Q^2 dependent. The lowest order vacuum polarization corrections responsible for this behaviour are shown in Fig. A.2(a). This figure shows a second kind of correction term, reflecting the fact that gluons carry color charge and can therefore couple to each other. Since photons do **not** carry electric charge these terms do not exist in QED. All possible higher order vacuum polarization terms together can be calculated using renormalization, resulting in the following expression for the *running*

[1] Theoretically, for an astronomically large (though finite) Q^2, the observed charge will go to infinity. This is called ultraviolet-divergence.

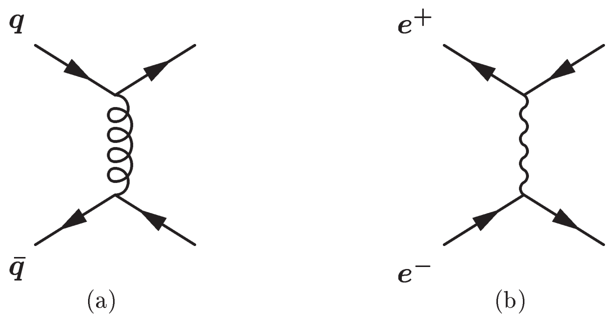

Figure A.1: Lowest order Feynman diagrams for $q\bar{q}$ interaction (a) and e^+e^- interaction (b).

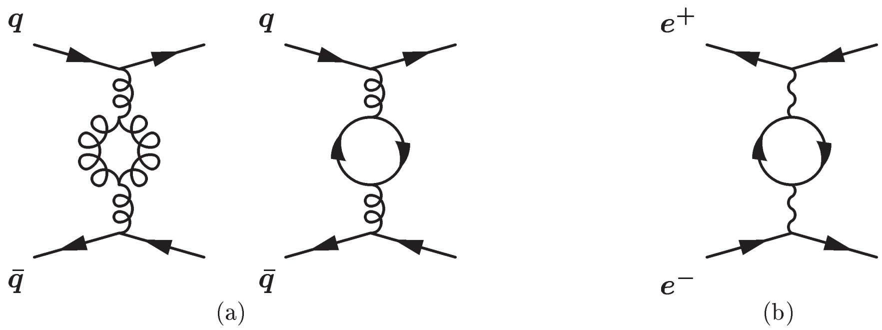

Figure A.2: Lowest order vacuum polarization corrections for $q\bar{q}$ interaction (a) and e^+e^- interaction (b).

coupling constant:

$$\alpha_s(Q^2) \approx \alpha_s\Big\{1 - \frac{7\alpha_s}{4\pi}\log\Big(\frac{Q^2}{\mu^2}\Big) + \Big[\frac{7\alpha_s}{4\pi}\log\Big(\frac{Q^2}{\mu^2}\Big)\Big]^2 + \dots\Big\} \tag{A.1}$$

$$\approx \frac{\alpha_s}{1 + (\alpha_s 7/4\pi)\log(Q^2/\mu^2)} \qquad (Q^2 \gg \mu^2), \tag{A.2}$$

where μ^2 is the value of Q^2 at which α_s is measured (corresponding to an effective charge). From expression A.2 one can see that $\alpha_s(Q^2) \to 0$ as $Q^2 \to \infty$. This reflects the fact that quarks and gluons appear to be free particles when probed with high Q^2. They have *asymptotic freedom*, the opposite of the ultraviolet-divergence in QED.

Eq. (A.2) also shows that for Q^2 becoming smaller, the color field becomes stronger. This equation makes a second interpretation of Q^2 possible. Apart from giving a measure of the resolution in a scattering experiment, it can be used more general as a measure of the strength of the color field. Therefore, Q^2 can also be used, for example, to specify the strength with which a quark and an antiquark are bound in a meson.

Using a Fourier transform the coupling constant can be re-expressed as a function of r, the distance between a quark and an antiquark.

$$\alpha_s(r) \approx \frac{1}{(7/2\pi)\log(1/\Lambda r)}\ , \qquad \Lambda^2 \equiv \mu^2 \exp(-4\pi/7\alpha_s) \tag{A.3}$$

This expression shows that the interaction becomes larger at increasing distance between the color charges. In Fig. A.3 the color field between a $q\bar{q}$ pair is compared with the electric field between a e^+e^- pair. From this figure it is

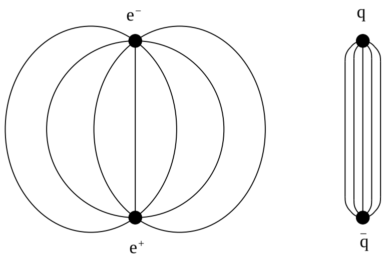

Figure A.3: The e^+e^- Coulomb field and the $q\bar{q}$ color field. Due to the gluon self-coupling the field lines group into a tube-like string.

possible to get a qualitative understanding of confinement. The color field lines attract each other because of the gluon self-interaction (second diagram in Fig. A.2(a)). When the separation between the color charges is increased the field density per unit length will remain the same. As a consequence the interaction strength will increase. This makes it impossible for a single quark to appear as a free unbound particle, i.e. the quark is a confined particle. Fig. A.3 shows the opposite behaviour for QED. If the distance between *electric* charges is increased the distance between the field lines will spread out, causing the attraction to become weaker

Feynman diagrams for QCD interactions can also be calculated using perturbation expansions (pQCD), equivalent with QED. But this expansion also only converges for a coupling constant smaller than one (approximately). This is exactly what makes the calculation of the hadronization process so difficult. It takes place at relatively small Q^2 (large distances between the quarks) and in that kinematic region the coupling constant will become large, making a pQCD calculation impossible.

Appendix B

Data tables

B.1 Krypton

ν	R_{att}	$\langle z \rangle$
2.615	0.627 ± 0.022	0.624
3.558	0.611 ± 0.014	0.553
4.529	0.647 ± 0.012	0.513
5.511	0.670 ± 0.011	0.490
6.504	0.677 ± 0.011	0.468
7.491	0.697 ± 0.013	0.447
8.730	0.748 ± 0.015	0.422

ν	R_{att}	$\langle z \rangle$
3.637	0.492 ± 0.030	0.828
4.570	0.499 ± 0.019	0.747
5.528	0.548 ± 0.016	0.678
6.524	0.557 ± 0.015	0.610
7.513	0.598 ± 0.017	0.557
8.748	0.659 ± 0.019	0.497

Table B.1: Attenuation ratio versus ν on a ^{84}Kr target for charged hadrons (left) and charged pions (right).

z	R_{att}	$\langle \nu \rangle$
0.165	0.827 ± 0.022	7.841
0.256	0.756 ± 0.012	7.053
0.351	0.687 ± 0.011	6.529
0.448	0.665 ± 0.011	6.211
0.546	0.632 ± 0.012	6.009
0.645	0.647 ± 0.015	5.893
0.744	0.570 ± 0.015	5.882
0.845	0.598 ± 0.018	5.738
0.940	0.514 ± 0.020	5.535

z	R_{att}	$\langle \nu \rangle$
0.275	0.620 ± 0.056	9.194
0.360	0.637 ± 0.020	8.192
0.452	0.588 ± 0.016	7.431
0.551	0.569 ± 0.016	6.905
0.646	0.570 ± 0.017	6.635
0.745	0.512 ± 0.017	6.357
0.846	0.549 ± 0.019	6.035
0.940	0.457 ± 0.020	5.768

Table B.2: Attenuation ratio versus z on a ^{84}Kr target for charged hadrons (left) and charged pions (right)

ν	R_{att}	$\langle z \rangle$
2.613	0.639 ± 0.025	0.621
3.551	0.638 ± 0.018	0.543
4.531	0.689 ± 0.016	0.504
5.507	0.693 ± 0.015	0.484
6.503	0.705 ± 0.015	0.463
7.491	0.727 ± 0.017	0.444
8.719	0.775 ± 0.019	0.423

ν	R_{att}	$\langle z \rangle$
2.622	0.588 ± 0.042	0.634
3.577	0.552 ± 0.024	0.576
4.525	0.572 ± 0.019	0.532
5.517	0.629 ± 0.019	0.501
6.507	0.632 ± 0.019	0.475
7.491	0.651 ± 0.020	0.453
8.748	0.709 ± 0.022	0.422

Table B.3: Attenuation ratio versus ν on a ^{84}Kr target for h^+ (left) and h^- (right).

ν	R_{att}	$\langle z \rangle$
3.653	0.462 ± 0.038	0.814
4.565	0.512 ± 0.026	0.743
5.520	0.537 ± 0.022	0.676
6.521	0.567 ± 0.021	0.606
7.523	0.610 ± 0.023	0.555
8.740	0.665 ± 0.024	0.497

ν	R_{att}	$\langle z \rangle$
3.618	0.532 ± 0.048	0.843
4.577	0.483 ± 0.028	0.751
5.538	0.563 ± 0.025	0.680
6.527	0.545 ± 0.023	0.615
7.501	0.583 ± 0.025	0.559
8.758	0.651 ± 0.026	0.497

Table B.4: Attenuation ratio versus ν on a ^{84}Kr target for π^+ (left) and π^- (right).

z	R_{att}	$\langle \nu \rangle$
0.165	0.875 ± 0.031	7.845
0.257	0.805 ± 0.017	6.980
0.351	0.723 ± 0.014	6.445
0.448	0.696 ± 0.015	6.086
0.545	0.643 ± 0.016	5.887
0.644	0.672 ± 0.019	5.724
0.745	0.597 ± 0.021	5.790
0.844	0.597 ± 0.024	5.687
0.939	0.494 ± 0.026	5.509

z	R_{att}	$\langle \nu \rangle$
0.165	0.756 ± 0.034	7.834
0.254	0.681 ± 0.019	7.185
0.350	0.627 ± 0.017	6.692
0.449	0.610 ± 0.018	6.462
0.549	0.612 ± 0.021	6.243
0.646	0.602 ± 0.024	6.226
0.743	0.525 ± 0.025	6.060
0.846	0.599 ± 0.030	5.820
0.942	0.546 ± 0.034	5.572

Table B.5: Attenuation ratio versus z on a ^{84}Kr target for h^+ (left) and h^- (right)

z	R_{att}	$\langle \nu \rangle$
0.275	0.707 ± 0.090	9.121
0.361	0.651 ± 0.028	8.177
0.451	0.600 ± 0.022	7.418
0.550	0.562 ± 0.022	6.869
0.645	0.572 ± 0.024	6.566
0.746	0.531 ± 0.024	6.339
0.845	0.550 ± 0.027	6.109
0.938	0.425 ± 0.026	5.800

z	R_{att}	$\langle \nu \rangle$
0.275	0.527 ± 0.075	9.299
0.360	0.621 ± 0.030	8.212
0.453	0.573 ± 0.024	7.448
0.552	0.578 ± 0.025	6.948
0.648	0.566 ± 0.026	6.722
0.743	0.489 ± 0.026	6.381
0.846	0.548 ± 0.029	5.946
0.942	0.498 ± 0.033	5.732

Table B.6: Attenuation ratio versus z on a ^{84}Kr target for π^+ (left) and π^- (right)

B.2 Nitrogen

ν	R_{att}	$\langle z \rangle$
2.614	0.878 ± 0.028	0.627
3.548	0.842 ± 0.017	0.558
4.524	0.889 ± 0.015	0.525
5.513	0.881 ± 0.014	0.503
6.501	0.892 ± 0.014	0.485
7.489	0.916 ± 0.015	0.465
8.712	0.944 ± 0.016	0.430

ν	R_{att}	$\langle z \rangle$
3.619	0.742 ± 0.039	0.830
4.558	0.834 ± 0.027	0.747
5.524	0.837 ± 0.022	0.683
6.517	0.886 ± 0.021	0.620
7.497	0.909 ± 0.022	0.570
8.727	0.936 ± 0.023	0.501

Table B.7: Attenuation ratio versus ν on a ^{14}N target for charged hadrons (left) and charged pions (right).

z	R_{att}	$\langle \nu \rangle$
0.165	0.898 ± 0.024	7.893
0.257	0.894 ± 0.014	7.052
0.352	0.886 ± 0.013	6.491
0.448	0.885 ± 0.014	6.144
0.545	0.844 ± 0.015	5.961
0.646	0.890 ± 0.019	5.903
0.746	0.858 ± 0.021	5.857
0.845	0.885 ± 0.024	5.727
0.940	0.777 ± 0.027	5.561

z	R_{att}	$\langle \nu \rangle$
0.275	0.840 ± 0.070	9.218
0.362	0.889 ± 0.025	8.190
0.452	0.858 ± 0.021	7.395
0.548	0.847 ± 0.021	6.860
0.648	0.871 ± 0.023	6.598
0.747	0.846 ± 0.024	6.341
0.845	0.880 ± 0.027	6.027
0.940	0.756 ± 0.028	5.767

Table B.8: Attenuation ratio versus z on a ^{14}N target for charged hadrons (left) and charged pions (right)

ν	R_{att}	$\langle z \rangle$
2.606	0.900 ± 0.032	0.632
3.542	0.864 ± 0.022	0.556
4.519	0.932 ± 0.020	0.517
5.507	0.907 ± 0.018	0.495
6.500	0.913 ± 0.018	0.483
7.486	0.933 ± 0.020	0.467
8.704	0.972 ± 0.022	0.430

ν	R_{att}	$\langle z \rangle$
2.644	0.811 ± 0.053	0.609
3.563	0.793 ± 0.031	0.564
4.532	0.810 ± 0.024	0.540
5.523	0.835 ± 0.023	0.518
6.501	0.857 ± 0.023	0.490
7.493	0.889 ± 0.025	0.461
8.724	0.903 ± 0.026	0.430

Table B.9: Attenuation ratio versus ν on a ^{14}N target for h^+ (left) and h^- (right)

ν	R_{att}	$\langle z \rangle$
3.609	0.809 ± 0.056	0.830
4.564	0.856 ± 0.037	0.744
5.511	0.838 ± 0.029	0.679
6.520	0.907 ± 0.029	0.620
7.492	0.918 ± 0.031	0.577
8.714	0.964 ± 0.031	0.497

ν	R_{att}	$\langle z \rangle$
3.634	0.654 ± 0.056	0.831
4.549	0.807 ± 0.040	0.751
5.541	0.836 ± 0.033	0.689
6.514	0.859 ± 0.032	0.621
7.503	0.898 ± 0.033	0.562
8.744	0.902 ± 0.033	0.505

Table B.10: Attenuation ratio versus ν on a ^{14}N target for π^+ (left) and π^- (right)

z	R_{att}	$\langle \nu \rangle$
0.165	0.920 ± 0.032	7.885
0.257	0.929 ± 0.019	6.989
0.352	0.917 ± 0.017	6.410
0.448	0.908 ± 0.018	6.038
0.545	0.863 ± 0.019	5.847
0.646	0.900 ± 0.024	5.766
0.746	0.890 ± 0.027	5.723
0.845	0.910 ± 0.032	5.630
0.940	0.791 ± 0.035	5.493

z	R_{att}	$\langle \nu \rangle$
0.165	0.865 ± 0.038	7.906
0.256	0.840 ± 0.022	7.159
0.351	0.834 ± 0.020	6.640
0.449	0.845 ± 0.023	6.346
0.545	0.808 ± 0.025	6.183
0.646	0.872 ± 0.031	6.155
0.748	0.802 ± 0.033	6.110
0.844	0.845 ± 0.038	5.893
0.939	0.754 ± 0.043	5.672

Table B.11: Attenuation ratio versus z on a ^{14}N target for h^+ (left) and h^- (right)

z	R_{att}	$\langle \nu \rangle$
0.275	0.941 ± 0.110	9.215
0.363	0.919 ± 0.035	8.194
0.452	0.866 ± 0.028	7.393
0.549	0.874 ± 0.029	6.796
0.648	0.864 ± 0.031	6.562
0.747	0.870 ± 0.034	6.333
0.846	0.911 ± 0.038	5.999
0.940	0.767 ± 0.039	5.743

z	R_{att}	$\langle \nu \rangle$
0.275	0.731 ± 0.094	9.221
0.361	0.852 ± 0.037	8.184
0.452	0.848 ± 0.031	7.397
0.546	0.813 ± 0.031	6.943
0.648	0.881 ± 0.036	6.643
0.748	0.817 ± 0.036	6.351
0.844	0.843 ± 0.039	6.064
0.939	0.742 ± 0.043	5.799

Table B.12: Attenuation ratio versus z on a ^{14}N target for π^+ (left) and π^- (right)